YALE
PEABODY
MUSEUM

JOURNAL OF MARINE RESEARCH

The *Journal of Marine Research,* one of the oldest journals in American marine science, published important peer-reviewed original research on a broad array of topics in physical, biological, and chemical oceanography vital to the academic oceanographic community in the long and rich tradition of the Sears Foundation for Marine Research at Yale University.

An archive of all issues from 1937 to 2021 (Volume 1–79) are available through EliScholar, a digital platform for scholarly publishing provided by Yale University Library at https://elischolar.library.yale.edu/.

Requests for permission to clear rights for use of this content should be directed to the authors, their estates, or other representatives. The *Journal of Marine Research* has no contact information beyond the affiliations listed in the published articles. We ask that you provide attribution to the *Journal of Marine Research.*

Yale University provides access to these materials for educational and research purposes only. Copyright or other proprietary rights to content contained in this document may be held by individuals or entities other than, or in addition to, Yale University. You are solely responsible for determining the ownership of the copyright, and for obtaining permission for your intended use. Yale University makes no warranty that your distribution, reproduction, or other use of these materials will not infringe the rights of third parties.

Eigenanalysis of the two-dimensional wind-driven ocean circulation problem

by V. A. Sheremet[1,2], G. R. Ierley[1] and V. M. Kamenkovich[2,3]

ABSTRACT

A barotropic model of the wind-driven circulation in the subtropical region of the ocean is considered. A no-slip condition is specified at the coasts and slip at the fluid boundaries. Solutions are governed by two parameters: inertial boundary-layer width; and viscous boundary-layer width. Numerical computations indicate the existence of a wedge-shaped region in this two-dimensional parameter space, where three steady solutions coexist. The structure of the steady solution can be of three types: boundary-layer, recirculation and basin-filling-gyre. Compared to the case with slip conditions (Ierley and Sheremet, 1995) in the no-slip case the wedge-shaped region is displaced to higher Reynolds numbers.

Linear stability analysis of solutions reveals several classes of perturbations: basin modes of Rossby waves, modes associated with the recirculation gyre, wall-trapped modes and a "resonant" mode. For a standard subtropical gyre wind forcing, as the Reynolds number increases, the wall-trapped mode is the first one destabilized. The resonant mode associated with disturbances on the southern side of the recirculation gyre is amplified only at larger Reynolds number, nonetheless this mode ultimately provides a stronger coupling between the mean circulation and Rossby basin modes than do the wall-trapped modes.

1. Introduction

In the present paper we consider the barotropic vorticity equation

$$\frac{\partial}{\partial t} \nabla^2 \psi + \delta_I^2 J(\psi, \nabla^2 \psi) + \frac{\partial \psi}{\partial x} = \delta_M^3 \nabla^4 \psi - \sin \pi y \tag{1.1}$$

in a square region $0 \leq x \leq 1$; $0 \leq y \leq 1$ with the following boundary conditions

$$\psi = 0; \quad \frac{\partial \psi}{\partial x} = 0 \quad \text{at } x = 0 \text{ and } x = 1 \tag{1.2a}$$

$$\psi = 0; \quad \frac{\partial^2 \psi}{\partial y^2} = 0 \quad \text{at } y = 0 \text{ and } y = 1. \tag{1.2b}$$

1. Scripps Institution of Oceanography, La Jolla, California, 92093-0230, U.S.A.
2. On leave from: P. P. Shirshov Institute of Oceanology, Russian Academy of Sciences, 23 Krasikova St., Moscow 117218, Russia.
3. Lamont-Doherty Earth Observatory of Columbia University, Palisades, New York, 10964, U.S.A.

Eq. (1.1) is written in a nondimensional form; ψ is the stream function; the axis x is directed to the east; the axis y is directed to the north; t is time; $J(a, b)$ is the Jacobian of the functions a and b with respect to x and y, ∇^2 is the Laplacian operator on the (x, y) plane; the square $0 \le x \le 1$; $0 \le y \le 1$ models a region of the subtropical gyre formation. One assumes that the curl of the wind stress in the region can be approximated by $-\sin \pi y$; δ_I and δ_M are nondimensional parameters characterizing the widths of inertial and viscous boundary layers respectively; $\delta_I = (\sqrt{U/\beta})/L$, $\delta_M = (\sqrt[3]{A_L/\beta})/L$, where A_L is the coefficient of lateral turbulent friction; U is a scale of the velocity in the open ocean governed by the Sverdrup relation; β is the latitudinal variation of the Coriolis parameter, L is the scale of the basin. We use impermeability and no-slip conditions (1.2a) at the coasts and impermeability and slip conditions (1.2b) at the fluid boundaries. For the initial value problem the stream function ψ should be specified at $t = 0$.

Geophysically meaningful values of the parameters δ_I, δ_M lie in the domain $0 \le \delta_I \le 0.1$; $0 \le \delta_M \le 0.1$. It is convenient to introduce the Reynolds number for the boundary layer

$$R = \frac{U(\delta_I L)}{A_L} = \left(\frac{\delta_I}{\delta_M}\right)^3 . \tag{1.3}$$

The problem (1.1), (1.2) has been extensively studied for many years in connection with the Gulf Stream and the subtropical gyre dynamics. To a certain degree this paper is a continuation of Ierley and Sheremet (1995), Kamenkovich *et al.* (1995) and Sheremet *et al.* (1995) (hereafter IS, KSPB, and SKP, respectively). These papers give an extensive list of relevant references.

As is well known, one of the most interesting features of the Gulf Stream system is the existence of a recirculation gyre following separation of the boundary current from the coast. According to observation (Halkin and Rossby, 1985; Hall, 1986) the transport of the gyre is about three times bigger than the transport of the Gulf Stream proper. Numerical evidence suggests that a noticeable gyre forms at $R > R_C$ where R_C is a critical value; for such values of R the steady boundary-layer type solution of the problem (1.1), (1.2) becomes unstable (Bryan, 1963; KSPB, SKP). In what sense should we understand the persistence of the recirculation gyre? Is it the primary circulation characteristic of the steady flow; or is it a secondary circulation driven by eddies? What is the basic physical mechanism responsible for the maintenance of the recirculation gyre: the effect of bottom topography, local wind forcing or advection of potential (absolute) vorticity in the western boundary current? An analysis of the time-dependent solutions of the problem (1.1), (1.2) indicates the existence of a quasi-stationary regime when the total kinetic energy oscillates (regularly or irregularly) around some constant value. Does such a behavior persist for the whole range of geophysically relevant parameters δ_I, δ_M? If yes, we can define a "steady" solution by the time-mean quasi-stationary regime? These questions drive us to the more general question of the dependence of the solution of the problem on the value of the coefficient of the lateral turbulent friction A_L. The smaller is the coefficient A_L, the richer is the instability of the physical system. Is it possible to have a saturated state, i.e., one in

which the solution is almost independent of the variation of A_L? Are the characteristics of such a solution geophysically relevant?

Not all of these questions are addressed to an equal extent in the present paper. Our main purpose is to analyze steady solutions of the problem (1.1), (1.2) in the geophysically reasonable range of parameters δ_I, δ_M: their existence, their structure and their stability. It will be demonstrated that such a study significantly clarifies the behavior of the time-dependent solutions of the problem.

Veronis (1963) was the first to argue for the possible existence of multiple steady states of the two-dimensional vorticity equation with bottom friction using a method of low-mode approximation. Il'in and Kamenkovich (1964) found that the steady one-dimensional boundary-layer type solution of the problem stemming from (1.1), (1.2) ceases to exist when the Reynolds number exceeds a critical value (see also Kamenkovich, 1966). To explain their arguments consider a particular solution to (1.1) of the form

$$\psi = (by + c)F(x) \tag{1.4}$$

where b and c are constants. Relation (1.4) represents the first term in the expansion of a solution of (1.1), (1.2) with respect to y near boundaries of the region $y = 0$ and $y = 1$. Substituting (1.4) into (1.1), approximating $\sin \pi y$ by πy near $y = 0$ and by $-\pi(y - 1)$ near $y = 1$ and assuming that a steady boundary-layer type solution exists gives the equation for the boundary layer at the western coast ($x = 0$).

$$b(F'^2 - FF'') + F - 1 = \frac{1}{R} F'''. \tag{1.5}$$

The boundary conditions follow from (1.2a)

$$F(0) = 0; \qquad F'(0) = 0; \qquad F(\infty) = 1 \tag{1.6}$$

where primes denote differentiation with respect to $\xi = x/\delta_I$, $b = \pi$ at the southern limit of the basin and $b = -\pi$ at the northern limit of the basin. Il'in and Kamenkovich (1964) showed numerically that in the case of $b < 0$ (northern part of the basin) there is a critical value of the Reynolds number R_{cr} such that the problem (1.5), (1.6) has two solutions for $R < R_{cr}$ that coalesce for $R = R_{cr}$ ($R_{cr} = 0.13$). Based on this evidence Il'in and Kamenkovich argued that for $R > R_{cr}$ the problem (1.5), (1.6) has no solution at all. They also suggested the same result is true of the full two-dimensional problem. The subsequent extensive analysis of (1.5) both for no-slip conditions ($F(0) = 0$; $F'(0) = 0$) and slip conditions ($F(0) = 0$; $F''(0) = 0$), incorporating the investigation of the stability of solutions, was given by Ierley and Ruehr (1986). Ierley (1987) suggested that the existence of a critical value of the Reynolds number R_{cr} is connected with the onset of recirculation in the northwest corner of the region for $R > R_{cr}$. It is thus evident that the appearance of a recirculation gyre destroys the boundary-layer character of the steady solution of (1.1).

There is another argument in favor of the nonexistence of steady solutions of (1.1), (1.2) of the boundary-layer type for large values of R (Kamenkovich, 1966). It is possible to

show that the solution of the inertial boundary layer equation has a singularity at a finite value of $\xi = \xi_0$ ($\xi = x/\delta_I$) when $y \rightarrow (1/2)^-$, or more precisely

$$\frac{\partial^2 u(\xi_0, y)}{\partial y^2} = O\left(\frac{1}{\sqrt{1/2 - y}}\right); \qquad \frac{\partial^2 v(\xi_0, y)}{\partial y^2} = O\left(\frac{1}{\sqrt{1/2 - y}}\right); \qquad (1.7)$$

where u, v are the components of the velocity. Since for the large values of R and $y < 1/2$ the influence of friction is confined to a very narrow coastal region of the width of $O(1/\sqrt{R})$ relations (1.7) are to be valid for the solution of the inertial-viscous boundary layer equation also. Therefore the friction terms $\nabla^2 u$ and $\nabla^2 v$ for such a solution would have a singularity at a finite value of ξ for large R which is impossible.

Is there a steady solution to (1.1), (1.2) not of boundary-layer type? Studying the problem with slip boundary conditions, Briggs (1980) found a new class of steady solutions of a basin-filling-gyre type. Strictly speaking such solutions were not found for geophysically relevant values of δ_I and δ_M: Briggs' values lie at the margin or even outside of geophysically meaningful range of the parameters. But Briggs' numerical experiments gave strong evidence that such solutions exist also for sufficiently small values of δ_I and δ_M such that $R \simeq 1$.

For the geophysically meaningful range of δ_I, δ_M the steady solutions of the basin-filling-gyre type for the slip problem were constructed in IS. It was found that for every δ_I, δ_M from this range there is at least one steady solution. The structure of the steady solution can be of three types: boundary-layer, recirculation and basin-filling-gyre types. However, for a certain subdomain of the parameters δ_I, δ_M the problem (1.1) with the slip boundary conditions has three steady solutions of indicated types simultaneously. The same result will be found here but for the no-slip case.

2. Steady solutions

It is natural to start with the analysis of steady solutions of the problem. We find the steady solution ψ_0 of the problem (1.1), (1.2) using an expansion of the stream function in Chebyshev polynomials and applying Newton's method for solving the resulting set of algebraic equations (the same method was used and discussed in IS; complete details of the Chebyshev method can be found in Boyd (1989)). In this way we can obtain steady solutions even when they are unstable.

The problem in nondimensional form has two parameters δ_I and δ_M characterizing intensity of wind forcing and viscous dissipation, respectively. But, the structure of a steady solution depends mainly on their ratio or basically the Reynolds number R. From the physical point of view, holding δ_I fixed and varying δ_M or R would be more appropriate since the lateral diffusivity is known very poorly while the wind forcing is relatively well determined. However, in order to illustrate the variation of steady solution in the parameter space it is more convenient to start with the case of fixed δ_M and varying δ_I or R since this case has two limiting solutions independent of R for small and large R. We note that the

psi_max=1.03

a) R=0.1, Low branch

psi_max=1.81

b) R=1.2, Low branch

psi_max=5.36

c) R=1.8785, Low nose

psi_max=13.06

d) R=1.5, Middle branch

psi_max=24.71

e) R=1.184, High nose

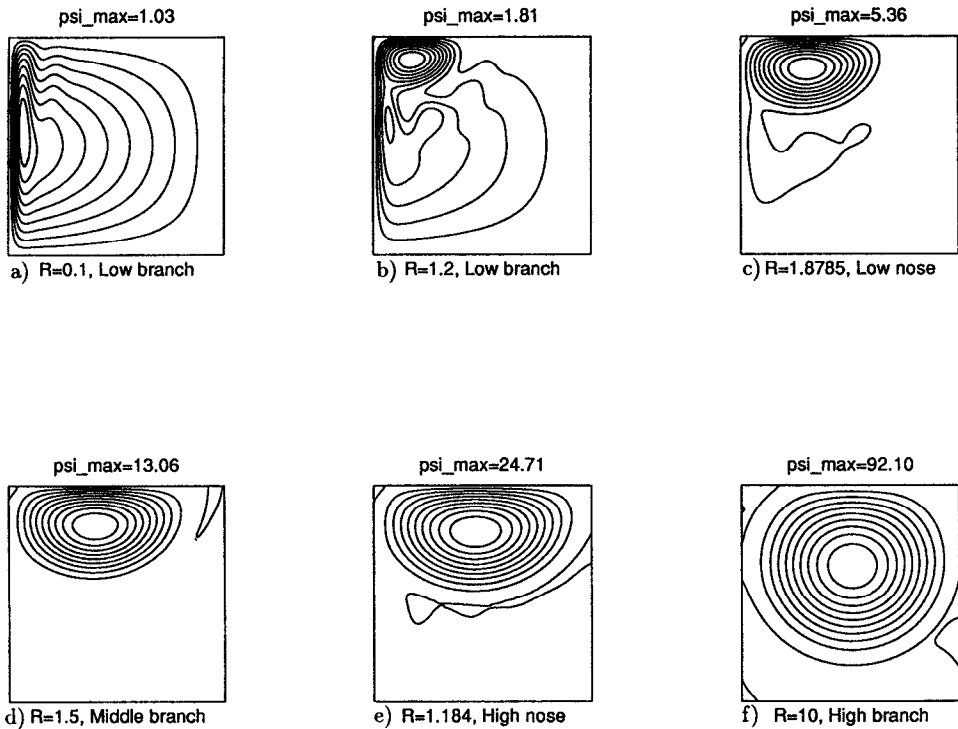psi_max=92.10

f) R=10, High branch

Figure 1. A sequence of the stream function patterns illustrating the transition from the linear Munk solution ($R \ll 1$) to the highly nonlinear basin-filling-gyre solution ($R \gg 1$) for fixed viscosity, $\delta_M = 0.02$, and varying Reynolds number, R. The no-slip boundary condition is applied at the coasts. The contour interval is $CI = 0.1$ max ψ. The transition is multivalued; between the low nose and high nose points the Reynolds number is decreasing.

numerical experiments with fixed δ_M usually require constant resolution dictated by the necessity to resolve thin viscous boundary layers.

In Figure 1 we present a sequence of stream function patterns corresponding to steady solutions with fixed $\delta_M = 0.02$ and varying R. In the linear case for small R the steady solution (Fig. 1, $R = 0.1$) is close to the Munk solution (Munk, 1950)

$$\psi_M(x, y) = \left((1 - x) - e^{-\xi/2} \left(\cos \frac{\sqrt{3}}{2} \xi + \frac{1}{\sqrt{3}} \sin \frac{\sqrt{3}}{2} \xi \right) \right) \sin \pi y + O(\delta_M), \qquad (2.1)$$

where $\xi = x/\delta_M$ is the stretched variable. Due to the beta-effect this solution has a boundary layer character and consists of a southward Sverdrup flow (Sverdrup, 1947) in the interior of the basin ($v \sim O(1)$) and an intense northward current ($v \sim O(1/\delta_M)$) along the western boundary which closes the pattern of circulation. The Munk solution has a maximum value of the stream function, $Q = 1 + \exp(-\xi_{max}) + O(\delta_M) = 1.16 + O(\delta_M)$, at $x = \xi_{max}\delta_M$, $\xi_{max} = 2\pi/3$, and $y = 1/2$ (the midpoint of the western boundary current).

In the highly nonlinear case for large R the steady solution ψ assumes the form of a single rapidly rotating gyre filling the whole basin (Fig. 1, $R = 10$). This solution was considered by Briggs (1980) for the problem with slip conditions at all boundaries. Common to both boundary conditions (slip and no-slip) the solution ψ approximately satisfies the defining relation

$$J(\psi, \delta_I^2 \nabla^2 \psi) = 0 \tag{2.2}$$

in the basin interior, which means that advection of relative vorticity dominates the dynamics or in other words the beta-effect becomes negligible. Scaling arguments and numerical experiments show that the maximum value of stream function, Q, asymptotes to a constant value $O(1/\delta_M^3)$ independent of δ_I for large R.

As the Reynolds number varies the most significant structural change in the solution happens around $R \simeq O(1)$ when an intense recirculation gyre forms in the northwest corner of the basin (Fig. 1b, c, d).

The maximum value of stream function, Q, providing a useful characterization of the solution, is plotted in Figure 2 as a function of R for several fixed values of δ_M. To make this plot we traced steady solutions by starting from the Munk solution (2.1) and varying R. As one can see, in a viscous regime ($\delta_M = 0.06, 0.08$) the function $Q(R)$ is single-valued, but for sufficiently small values of viscosity parameter, $\delta_M < \delta_{M_{NCusp}}$, becomes *multivalued*. This is seen in the S-shaped curves of Figure 2 for $\delta_M = 0.02, 0.03, 0.04$. In other words, there exist three different steady solutions within a certain range of R. According to the maximum value of the stream function Q we term the corresponding branches: low, middle, and high. The points where the branches meet each other we call low and high nose points; corresponding values of the Reynolds number will be called R_L and R_H.

In a three-dimensional space a surface given by $Q = Q(\delta_M, R)$ (or $Q(\delta_M, \delta_I)$) forms the so called Whitney tuck[4] (Whitney, 1955). If the points on this surface are projected onto the plane (δ_M, R) the region where three steady solutions coexist coincides with the wedge-shaped area shown by solid lines in Figure 3. The sides of the wedge are the projections of the folds of the tuck. The tip of the wedge is located at $\delta_{M_{NCusp}} = 0.04223$, $\delta_{I_{NCusp}} = 0.05637$ or $R_{NCusp} = 2.378$. At this point all three solutions coalesce in a *cusp* singularity. This situation is a typical example of the cusp catastrophe (Arnol'd, 1984, Ch. 2). The maximum value of the stream function at this point $Q_{NCusp} = 2.90$. The solution at the cusp is similar to one given in Figure 6 of IS but with increased values of relative vorticity present within viscous sublayers near the western and eastern boundaries.

Thus it turns out that the character of steady solutions in the problems with no-slip and slip boundary conditions at the east and west coasts is very similar. The reader is referred to IS where the problem with the slip conditions is thoroughly examined. Figure 1 from IS can serve as a schematic illustration of the Whitney tuck. Almost everything said in Section 3 of IS about steady solutions of the problem with slip conditions can be reiterated for the

---

4. "Tuck" is a word meaning a fold or a series of folds. It was borrowed from fabric design by mathematicians trying to distinguish the particular case of two merging folds from other possible arrangements of folds.
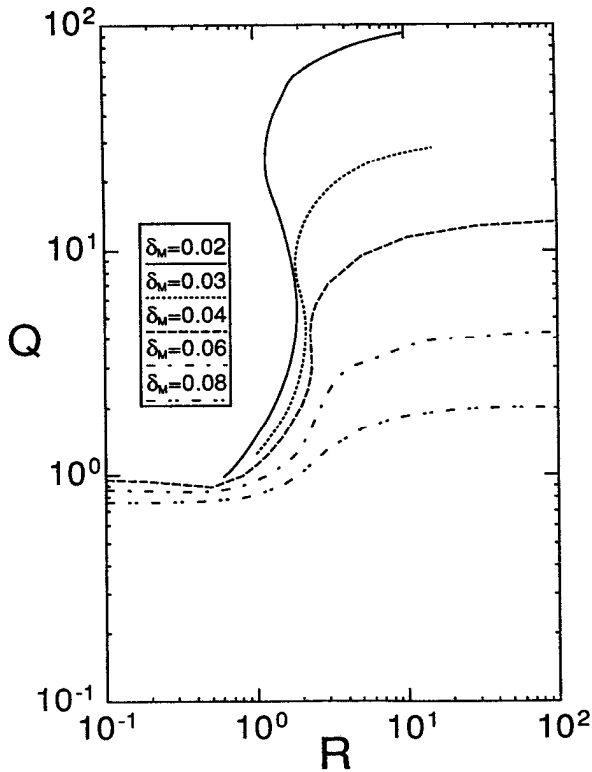
Figure 2. The dependence of the maximum of the stream function, Q, on the Reynolds number R for several values of viscosity, δ_M. For $\delta_M < \delta_{M_{Ncusp}} = 0.04223$ the function $Q(R)$ is multivalued corresponding to the 'S'-shaped transition from the linear to the highly nonlinear case. The curves are produced by connecting the calculated points by straight lines, without fitting or smoothing.

problem with no-slip conditions. This indicates the robustness of the cusp catastrophe of steady solutions of the problem with respect to boundary conditions.

Let us stress only differences between the problems with no-slip and slip conditions. For comparison the wedge-shaped area of multiple solutions in the problem with the slip conditions is shown by a dashed line in Figure 3. The cusp in the slip case is located at $\delta_{M_{SCusp}} = 0.555$, $\delta_{I_{SCusp}} = 0.6207$ ($R_{SCusp} = 1.3987$) with the maximum of the stream function $Q_{SCusp} = 3.46$. We see that the wedge in the no-slip case is displaced to larger Reynolds numbers as compared to the slip case. This is closely related to the growth of the recirculation gyre in the northwest corner of the basin. In the no-slip case the viscous forces are more efficient in decelerating western boundary current. Therefore a smaller recirculation gyre forms for the same R and the low branch solutions persist for larger R as compared to the slip case.

We also note that in the no-slip case the amplitude of the Briggs basin-filling-gyre (high branch) type solution is considerably smaller, by a factor of approximately 4.3. For
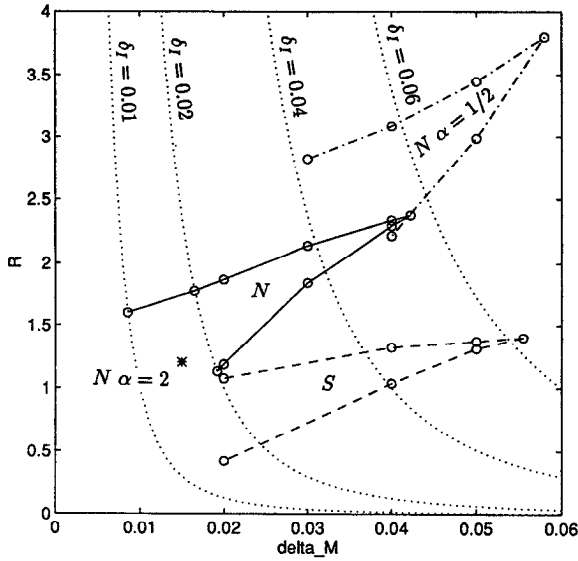
Figure 3. The locations of the region in the (δ_M, R)-plane where three solutions coexist for several cases. The wedge-shaped area shown by the solid line and indicated by the symbol N corresponds to the standard case with the no-slip conditions at the coasts and the aspect ratio $\alpha = 1$. The case with the slip conditions at all boundaries ($\alpha = 1$) is shown by the dashed line and the symbol S. The case with the no-slip conditions and the aspect ratio $\alpha = 1/2$ is shown by the dashed-dotted line and the symbol $N\alpha = 1/2$. The tentative location of the cusp of the wedge in the no-slip case with $\alpha = 2$ is marked by the asterisk. The small circles indicate the solutions at the low and high nose points in some experiments. The dotted lines correspond to $\delta_I = const$.

example for sufficiently large $R = 10$, the ratio $Q_{IG_{Slip}}/Q_{IG_{No\text{-}slip}} = 14.6/3.69 = 3.97$ for $\delta_M = 0.06$; $Q_{IG_{Slip}}/Q_{IG_{No\text{-}slip}} = 50.0/11.4 = 4.39$ for $\delta_M = 0.04$; $Q_{IG_{Slip}}/Q_{IG_{No\text{-}slip}} = 400/92.1 = 4.34$ for $\delta_M = 0.02$ and it varies only slightly with δ_M. We see that in both cases for $R \gg 1$ the maximum value of the stream function indeed asymptotically scales as $Q = C/\delta_M^3$, where in the no-slip case the constant $C = C_N = 0.74 \cdot 10^{-3}$ while in the slip case $C = C_S = 3.2 \cdot 10^{-3}$. For high branch solutions the difference in amplitude is again due to the viscous forces which bring the velocity to zero at the coasts and produce stress tangential to the boundary.

It is helpful to recall that in the slip case the net torque applied by the wind on the fluid is balanced by the torque of pressure forces (normal to the boundary) since tangential stress of viscous forces at the boundary is zero by definition. In the no-slip case the torque of the viscous stress tangential to the boundary is added to the balance (see Morgan, 1956). In a problem with a *circular* basin and slip boundary conditions the amplitude of the high branch solution becomes infinite as $R \to \infty$ for fixed δ_M since the net torque of pressure forces tends to zero as the beta-effect becomes less and less important and the stream lines become more and more circular. (Note that when boundary is not straight zero stress does not imply zero vorticity.) On the other hand in the no-slip case with circular geometry, the high branch solution exists, with an amplitude that approaches a limiting value of

$O(1/\delta_M^3)$. This reflects the balance between the wind forcing and lateral diffusion of vorticity while the torque of the boundary pressure forces goes to zero.

There is one reservation about the character of steady solutions in the no-slip case for large δ_I and small δ_M; the behavior is much richer than in the slip case. Careful computations reveal the existence of another fold near $\delta_I = 1$ associated with the existence of a gyre-type solution other than the Briggs result. There may be yet other singularities beyond the available model resolution. But we won't dwell upon the peculiarities of the solution in that part of the parameter space since our main interest lies within geophysically meaningful range $0 \leq \delta_M$, $\delta_I \leq 0.1$. The statement is that in the vicinity (say for $R < 50$) of the main Whitney tuck described above, the character of the steady solutions of the problem with no-slip and slip boundary conditions is the same.

We temporarily consider a more general problem with one more nondimensional parameter: aspect ratio α. To do this we replace the last term in (1.1) by $-\alpha \sin \pi y$ and consider a rectangular domain $0 \leq x \leq 1/\alpha$, $0 \leq y \leq 1$. Such introduction of the aspect ratio in the nondimensional problem is useful since the Sverdrup transport near the western coast and the balance of terms in the western boundary current remain independent of α. We argue that the formation of the recirculation gyre depends mainly on the dynamical balance of terms in the western boundary current. Figure 4 shows three steady solutions for the same $\delta_M = 0.02$, $R = 1$ but different $\alpha = 0.5, 1, 2$. These solutions belong to the low branch. We see that these solutions have the recirculation gyres of approximately the same size. It is obvious that the high branch solutions are more sensitive to the geometry of the basin. Numerical calculations show that for $\alpha = 0.5$ as Q increases the growing recirculation gyre extends all the way to the eastern coast and then extends south to occupy the whole basin similar to the scenario for $\alpha = 1$. For $\alpha = 2$, however, the recirculation gyre upon extending to the eastern coast remains concentrated near the northern boundary as its amplitude increases. (We traced solutions for R up to 500.)

The location of the wedge-shaped area of multiple solutions of the problem with no-slip conditions for $\alpha = 0.5$ is shown in Figure 3 by a dash-dotted line. We were unable to accurately trace the wedge for $\alpha = 2$ because of increased resolution required, but we found clear evidence that multiple solutions exist for $\alpha = 2$ as well. The maximum slope of Q as a function of R for fixed δ_M increases as we decrease the viscosity parameter δ_M. For illustrative purpose the location of the cusp itself can be found sufficiently accurately by extrapolating $dR/dQ(\delta_M, R)$ in the parameter space. In Figure 3 the tentative location of the cusp for $\alpha = 2$ is marked by an asterisk. Thus we can conclude that the cusp catastrophe is a quite robust feature of the barotropic vorticity equation surviving the variation of boundary conditions and basin geometry. We now return to our standard case with the aspect ratio $\alpha = 1$.

Crossing the tuck in direction of fixed δ_I also results in transition from low branch solutions to middle branch solutions and finally to high branch solutions. For the reader's convenience we show lines $\delta_I = const$ on Figure 3. We do not present plots of $Q(R)$ for fixed δ_I for the no-slip case because they look similar to the curves for the slip case in Figure 3 of IS.

$\alpha = 1 \ \psi_{max} = 1.49$ at $(0.149, 0.903)$ $\alpha = 2 \ \psi_{max} = 1.32$ at $(0.129, 0.907)$

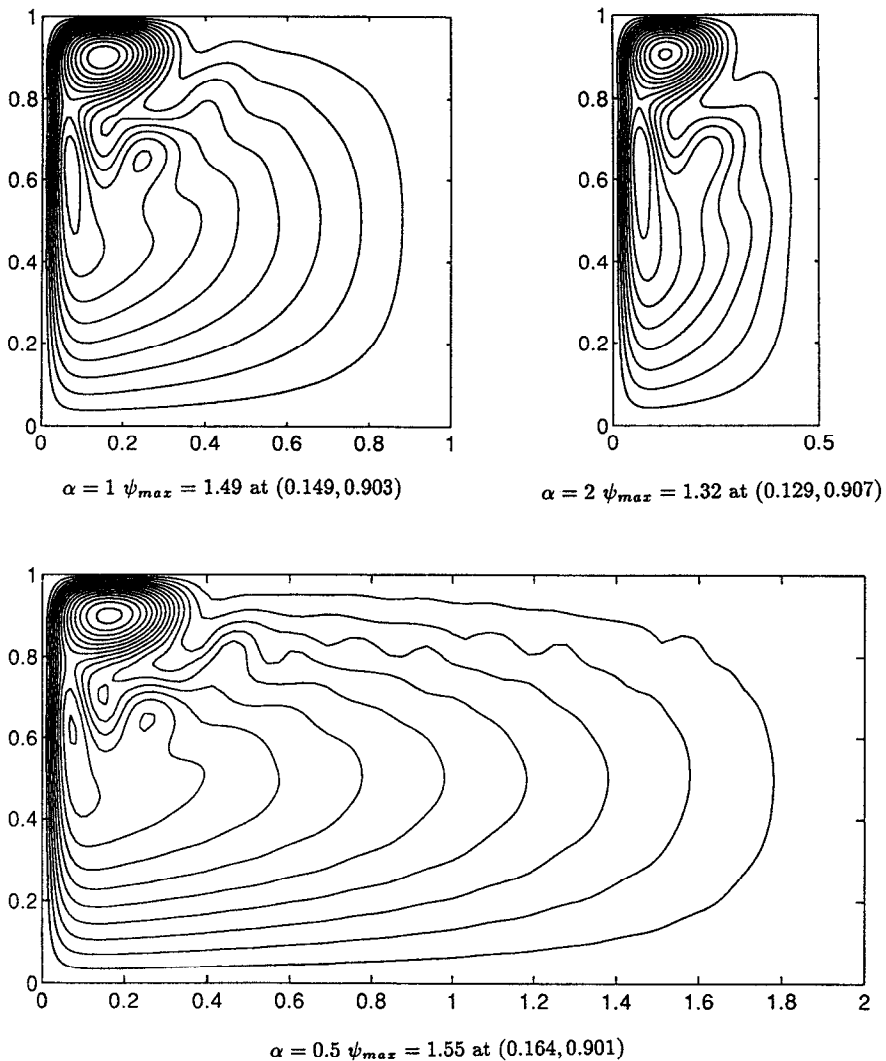$\alpha = 0.5 \ \psi_{max} = 1.55$ at $(0.164, 0.901)$

Figure 4. The steady solutions (belonging to the low branch) for the same parameters $\delta_I = 0.02$, $\delta_M = 0.02$, $R = 1$, no-slip but for three different values of the aspect ratio $\alpha = 1, 2, 1/2$.

Let us consider a case with $\delta_I = 0.01$ (no-slip conditions) which corresponds to the wind forcing typical for the North Atlantic subtropical gyre. A sequence of steady solutions belonging to the low branch for increasing values of Reynolds number R (thus decreasing viscosity) is shown in Figure 5. The most dramatic feature of this sequence is the formation of tight recirculation gyre in the northwest corner of the basin.

For small R the solution is essentially linear, dominated by viscosity, and close to the Munk solution (2.1). As the Reynolds number increases a separate gyre of the same size as the boundary layer thickness, $O(\delta_I)$, commences in the northwest corner for R about 0.4
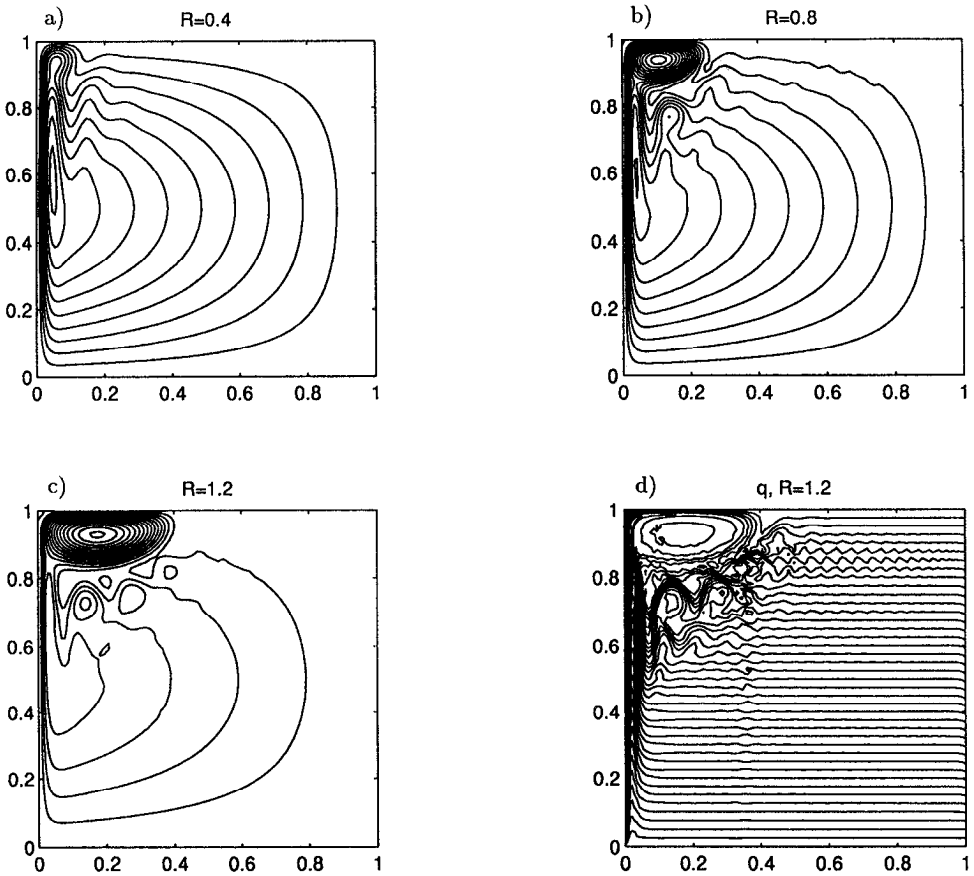
Figure 5. A sequence of the stream function patterns (a, b, c) illustrating the variation of steady (low branch) solution for the fixed $\delta_I = 0.01$ and increasing Reynolds number, $R = 0.4, 0.8, 1.2$. The contour interval is $CI = 0.1$ for $R = 0.4, 0.8$; $CI = 0.2$ for $R = 1.2$. The plot (d) shows the potential vorticity field $q = y + \delta_I^2 \nabla^2 \psi$ for $R = 1.2$.

(Fig. 5a). As R increases further (Fig. 5b, c) the recirculation develops into a strong gyre of considerable size and intensity. For $R = 1.2$, for example, the maximum transport of the recirculation gyre $Q = 3.02$. This particular steady solution of the barotropic model would be the most relevant for comparison with the real Gulf Stream system since according to observations the maximum transport of the Gulf Stream is approximately three times bigger than the Sverdrup transport (Halkin and Rossby, 1985; Hall, 1986). In the model the maximum eastward velocity in the recirculation gyre $u = 80$ is found at the northern boundary. On the southern side of the recirculation gyre the maximum westward velocity is $u = -35$. The maximum northward velocity within the western boundary current $v = 50$ at $x = 0.0125$, $y = 0.727$. To obtain dimensional velocities one has to multiply the above values by the velocity scale U, typically 3 cm s^{-1}.

The potential vorticity field $q = y + \delta_I \nabla^2 \psi$ for $R = 1.2$ is given in Figure 5d. One can see

that within the recirculation gyre q is more uniform than elsewhere in the basin and that the isolines of q and ψ nearly coincide, which indicates an inertial type of flow. Also, q slightly decreases centerward, apparently due to the negative input of the wind curl in this region (see IS). The interior of the recirculation gyre is surrounded by a layer of increased gradients of q, especially near the western and northern boundaries. The nondimensional variation of q from the center of the recirculation gyre to the northern boundary is about 0.17. Applied to the ocean such variation can be considered small and therefore the quasigeostrophic approximation, which is used in deriving the barotropic vorticity equation (1.1), is valid. It is also worth mentioning that the relative vorticity $\delta_I^2 \nabla^2 \psi$ is important only within western boundary layer and in the region around the recirculation gyre, and negligible in the interior of the basin where isolines of q are straight lines.

Following the low branch of steady solutions, the recirculation gyre keeps growing with increasing R until the low nose point is reached which for $\delta_I = 0.01$ is located at $R_L = 1.6$. For $R > R_L$ steady solutions of the boundary-layer type (dominated by the beta-effect) cease to exist. The only steady solution available is on the high branch, but it has much larger amplitude of both the stream function and energy. Therefore, for $R > R_L$ the solution of the initial value problem (1.1), (1.2) is likely not to stabilize with time. Whether or not a time- dependent solution will tend to the high branch or stay in the neighborhood of the low branch depends on many factors, for example, stability of the respective branches of steady solutions, which will be considered in the next section. It turns out that the steady solutions on the low branch become unstable for Reynolds number substantially smaller than R_L.

Before proceeding to the next section we have to note once more that the high branch solutions give unrealistically high velocities ($O(10$ m s^{-1} for the North Atlantic) throughout the gyre. But high branch solutions cannot be simply ignored; they are perfectly valid members of the continuous family of solutions of the barotropic vorticity equation. As we have seen the position of the cusp and the folds of the Whitney tuck strongly depend on the structure and amplitude of the high branch solutions. In the following sections, however, we will devote most of our attention to stability analysis of the lower branch solutions because they are more geophysically meaningful.

3. Stability of steady solutions and the structure of eigenmodes

The second logical step is to investigate the stability of steady solutions. We restrict ourselves to linear analysis assuming that the amplitude of perturbation is small.

Linearizing (1.1) about the steady solution ψ_0 or, in other words, taking a functional derivative of (1.1) with respect to ψ, and representing the perturbation ψ' as $\varphi(x, y) \exp(-i\sigma t)$ we obtain a spectral problem for the perturbation amplitude φ

$$-i\sigma \nabla^2 \varphi + \delta_I^2 [J(\psi_0, \nabla^2 \varphi) + J(\varphi, \nabla^2 \psi_0)] + \varphi_x = \delta_M^3 \nabla^4 \varphi \tag{3.1}$$

$$\varphi = 0 \quad \text{at } x = 0, \quad x = 1, \quad y = 0, \quad y = 1 \tag{3.1a}$$

$$\frac{\partial \varphi}{\partial x} = 0 \quad \text{at } x = 0, \quad x = 1 \quad \text{and} \quad \frac{\partial^2 \varphi}{\partial y^2} = 0 \quad \text{at } y = 0, \quad y = 1. \tag{3.1b}$$

Upon solving this spectral problem we obtain a set of eigenfrequencies σ_k and corresponding eigenfunctions φ_k. Numerically the eigenproblem is also solved (as in IS) using Chebyshev expansions of φ and ψ_0: in terms of the amplitudes of such an expansion φ', (3.1), (3.1a, b) reduces to a generalized eigenproblem $A\varphi' = -i\sigma B\varphi'$ in matrix form. Usually, the eigenfrequencies σ_k are complex since, in the presence of viscosity, the problem is not self-adjoint. The imaginary part of the frequency gives the rate of growth (or decay) of the perturbation.

As the parameters δ_M, δ_I vary, so does the steady solution ψ_0 as well as the eigenspectrum and the patterns of corresponding eigenfunctions. It is interesting to trace the changes following the low branch of steady solutions with fixed δ_I for increasing R. The steady solution ψ_0 for $\delta_I = 0.01$, $R = 0.4$ and $R = 0.8$ with no-slip conditions at the coasts is given in Figure 5a,b. These are typical solutions belonging to the low branch; we give their eigenspectra in Figure 6. From (3.1) it is clear that the eigenvalues $-i\sigma_k$ come in complex conjugate pairs and the corresponding eigenfunctions are also complex conjugates. Therefore it is sufficient to plot eigenfrequencies with $Re(\sigma_k) \geq 0$ only (Fig. 6). If $Re(\sigma_k) > 0$ then the eigenmode is oscillatory and its eigenfunction is complex. One can interpret the real part as the flow pattern at time zero and the imaginary part as the flow pattern a quarter of a period later. Thus comparing the real and imaginary parts one can determine the direction of propagation of the phase. For small Reynolds numbers the steady solution is stable, all eigenfrequencies have negative imaginary part $Im(\sigma_k) < 0$. For $R = 0.4$ there are two weakly growing eigenmodes (Fig. 6a). As the Reynolds number increases the eigenfrequencies of these growing modes shift further to the right while new eigenfrequencies cross the vertical axis $Im(\sigma) = 0$ and the corresponding eigenmodes start to grow too. In Figure 6b for $R = 0.8$ there are already four growing modes.

a. Basin modes of Rossby waves. Many of the eigenmodes corresponding to the eigenspectrum (Fig. 6) are easily identified with the basin modes of Rossby (planetary) waves.

First, recall that the idealized Rossby basin modes in a square region are the solutions of the inviscid ($\delta_M^3 = 0$) eigenproblem (3.1) with zero mean flow ($\delta_I^2 = 0$) and with boundary condition (3.1a) (Pedlosky, 1987).

$$\varphi_{nm}^{(0)}(x, y, t) = -1/4(e^{ik_2(x-1/2)} - e^{ik_1(x-1/2)})(e^{ily} - e^{-ily})e^{-i\sigma_{nm}^{(0)}t}$$

$$= \exp\left(-i\frac{(x-1/2)}{2\sigma_{nm}^{(0)}} - i\sigma_{nm}^{(0)}t\right) \sin(n\pi x)\sin(m\pi y), \quad (3.2)$$

where

$$k_{1,2} = -\frac{1}{2\sigma_{nm}^{(0)}} \pm n\pi, \qquad l = m\pi, \qquad \left(\frac{1}{2\sigma_{nm}^{(0)}}\right)^2 = (n^2 + m^2)\pi^2 \qquad (3.3)$$

$n, m = 1, 2, 3, \ldots$ denote harmonics in x and y, respectively.

Both viscosity and the mean flow ψ_0 (advection and nonuniform distribution of vorticity) modify the basin modes of Rossby waves. However, we should recall that in the ocean
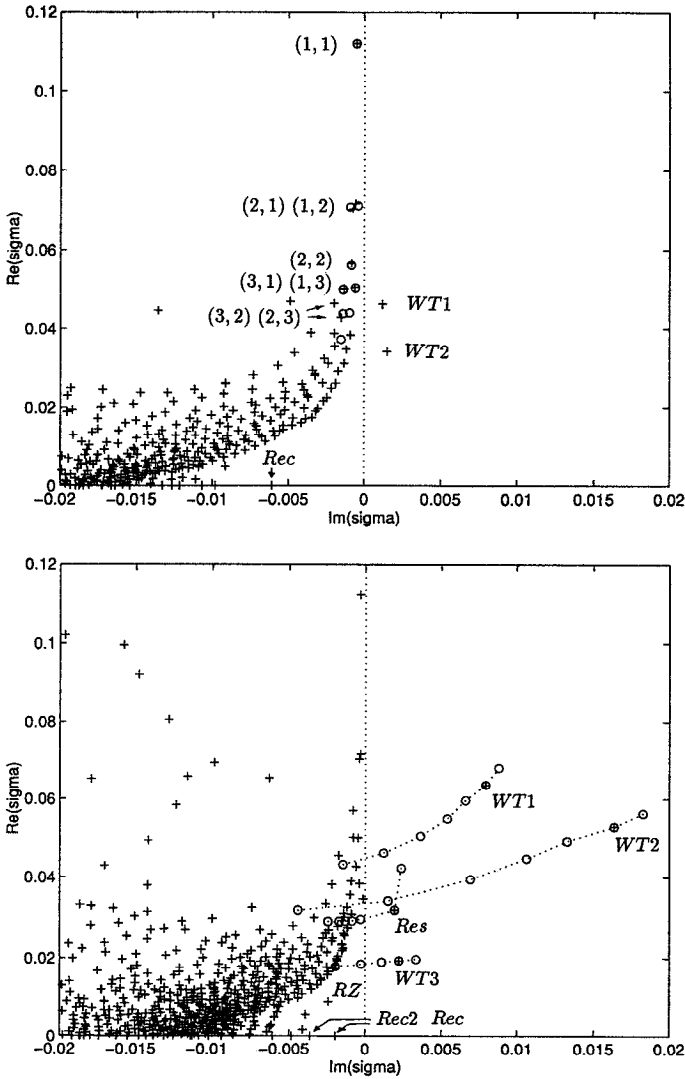
Figure 6. (a) The eigenspectrum corresponding to the steady solution for $\delta_I = 0.01$, $R = 0.4$ (see Fig. 5a). The crosses indicate eigenfrequencies. The eigenfrequencies corresponding to some lowest basin modes of Rossby waves are marked by indices (n, m). The circles indicate eigenfrequencies of nine $(n, m = 1, 2, 3)$ lowest basin modes as predicted by the perturbation theory without the mean flow. Two eigenfrequencies corresponding to the growing wall-trapped modes are marked by WT1, WT2. Rec points to the eigenfrequency with $Re(\sigma) = 0$ corresponding to the recirculation gyre mode. (b) The eigenspectrum corresponding to the steady solution for $\delta_I = 0.01$, $R = 0.8$ (see Fig. 5b). The crosses indicate eigenfrequencies. Four modes are growing: the wall-trapped modes WT1, WT2, WT3 and the resonant mode Res. The variation of the eigenfrequencies of these modes for $R = 0.3, 0.4, 0.5, 0.6, 0.7, 0.8, 0.9$ is shown by circles connected by dotted lines. Thus for $R = 0.8$ their eigenfrequencies are shown by a cross within circle. Rec marks the recirculation gyre mode; Rec2 marks the next harmonic. RZ indicates the recirculation zone mode.

away from the narrow western boundary currents, the group velocity of barotropic Rossby waves is significantly higher than the velocity of the mean circulation and therefore the dynamics of the Rossby waves in the interior of the ocean basin is almost linear and inviscid. Thus perturbation theory can be used to study the influence of viscosity and mean flow on the basin modes. We will use the term "idealized" to designate the unperturbed modes (3.2), (3.3).

The effect of viscosity alone can easily be addressed since in this case the partial differential equation (3.1) has constant coefficients. To a first approximation the perturbed eigenfunction is the sum of an interior part which is close to the idealized eigenfunction (3.2) and a boundary layer correction required to satisfy the dynamical boundary conditions (3.1b). If $\delta_M < \sigma_{nm}^{(0)}$ (in nondimensional form), then the beta-effect within the boundary layer can be neglected and the boundary layer correction will be an oscillatory Stokes boundary layer of thickness

$$\delta_f = \sqrt{\frac{2\delta_M^3}{\sigma_{nm}^{(0)}}} \tag{3.4}$$

(see, for example, Batchelor, 1967). We note that in the slip case this boundary layer correction of the same width δ_f also exists, but its effect is smaller since it is the relative vorticity that becomes zero at a (straight) boundary in the slip case rather than velocity in the no-slip.

Upon solving for the boundary layer correction we get a modified kinematic boundary condition for the interior part of the eigenfunction since it is the sum of the interior part and boundary layer correction that satisfies (3.1a). Also taking into account the dispersion relation for the Rossby waves modified by the viscous term in (3.1) we finally arrive at the formula for the shift of eigenfrequencies due to viscosity in the no-slip case

$$\Delta\sigma_{nm} = \sigma_{nm} - \sigma_{nm}^{(0)} = \sigma_{nm}^{(0)} \frac{n^2}{(n^2 + m^2)} (B + V) \tag{3.5}$$

$$B = \delta_f(-1 - i) \qquad V = -i \frac{\delta_M^3}{\sigma_{nm}^{(0)3}} \frac{2n^2 + m^2}{2n^2}, \tag{3.6}$$

where $\sigma^{(0)}$ is the unperturbed frequency of the idealized basin mode (3.3). Note that the Stokes boundary layer thickness δ_f depends on frequency and therefore is different for different basin modes. We see that there are two parts: a contribution from the boundary layer B and volume perturbations V from the interior. The boundary layer shifts not only the imaginary part of σ due to energy dissipation, but also the real part of σ since the length of the basin is effectively decreased by the thickness of the boundary layer δ_f (in analogy with the displacement thickness in the theory of Prandtl boundary layer).

In the no-slip case the boundary layer contribution is dominant $\Delta\sigma \simeq O(\delta_M^{3/2})$, the dissipation in the interior gives only $\Delta\sigma \simeq O(\delta_M^3)$. To obtain a formula for $\Delta\sigma$ in the slip
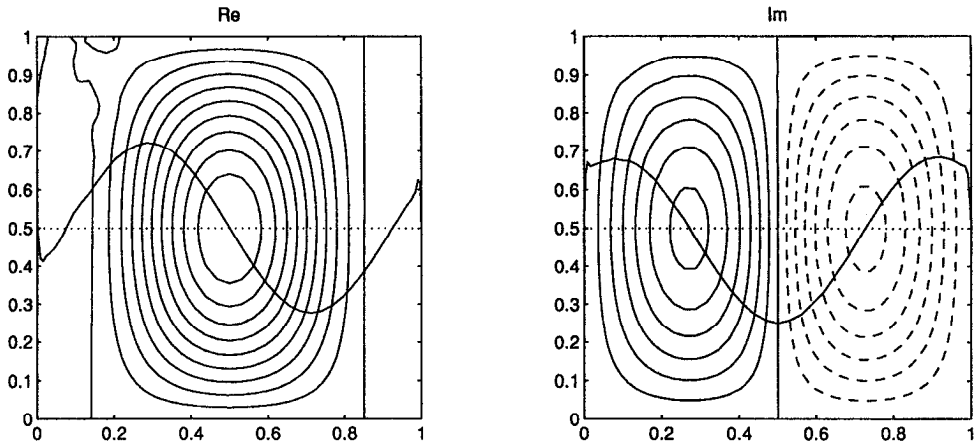
Figure 7. The Rossby eigenmode $\varphi_{11}(x, y)$, real and imaginary parts, corresponding to the steady solution ψ_0, $\delta_I = 0.01$, $R = 0.8$, no-slip. The contour interval $CI = 0.1$ max ($|\varphi_{11}|$). The negative isolines are dashed. Overlapped is the velocity profile $v(x) = \partial\varphi_{11}/\partial x$ for $y = 1/2$ (solid line) with zero $v(x) = 0$ shown by the dotted line.

case we simply cancel the boundary layer contribution and then the dissipation in the interior becomes dominant.

We compared the prediction from formula (3.5) with the decay rates of the basin modes obtained numerically for the eigenproblem without mean flow. The agreement is especially good for low basin modes for which the condition $\delta_M < \sigma_{nm}^{(0)}$ holds very well. In Figure 6a the locations of nine lowest eigenmodes of Rossby waves as predicted by the perturbation theory for the corresponding δ_M are indicated by circles.

Thus perturbation theory can satisfactorily explain the negative shift of the imaginary part of eigenfrequency of Rossby basin modes. As the viscosity decreases the eigenfrequencies get closer and closer to the axis $Im(\sigma) = 0$, but in the problem without mean flow the viscosity alone can never make the imaginary part of the eigenfrequency positive.

The effect of the mean flow can in principle also be addressed by the perturbation theory for $\delta_M \ll 1$ and $R \ll 1$, but the analysis is much more complicated since the steady state itself changes with R.

We present in Figure 7 the basin mode φ_{11}. We see that a slight alteration takes place in the northwest corner because of interaction with the recirculation gyre. Note that viscous Stokes sublayers form along the western and eastern boundaries, but they are not so conspicuous. To reveal these sublayers we plotted in Figure 7 the velocity profile $v(x) = \partial\varphi_{11}/\partial x$ for $y = 1/2$. For $\delta_I = 0.01$, $R = 0.8$ and $\sigma_{11}^{(0)} = 0.1125$, as in this case, $\delta_f = 4.71 \cdot 10^{-3}$ according to (3.4). We note that the Chebyshev expansion with $N_x = 51$ polynomials in x direction resolves such a thin boundary layer very well. The first
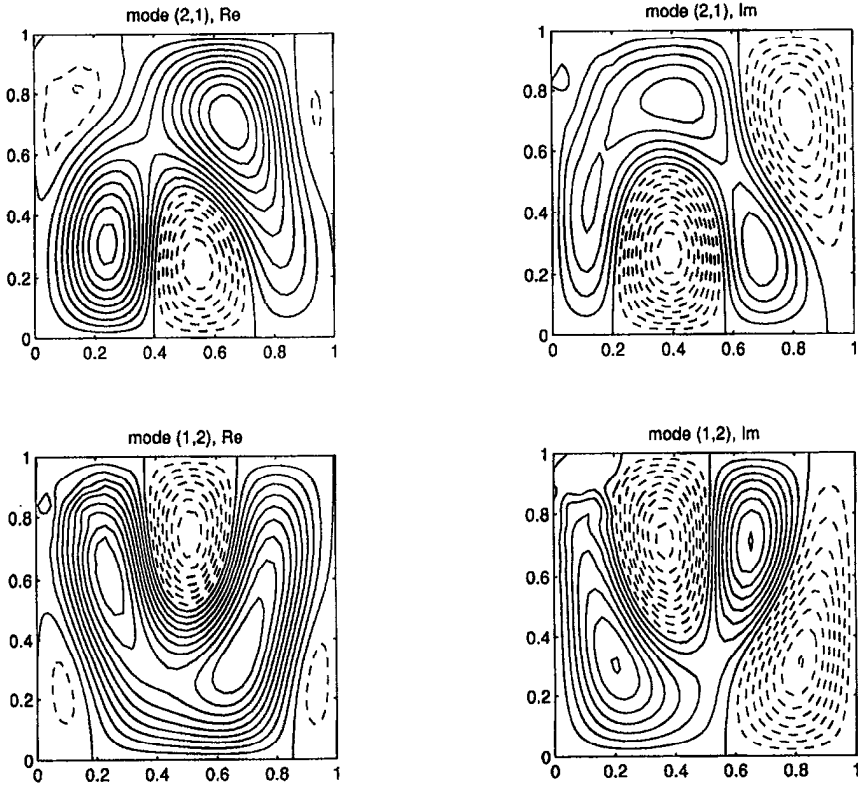
mode (2,1), Re

mode (2,1), Im

mode (1,2), Re

mode (1,2), Im

Figure 8. (a) The degenerate pair of Rossby eigenmodes $\varphi_{21}(x, y)$ and $\varphi_{12}(x, y)$. $CI = 0.1$ max $(|\varphi_{nm}|)$. The negative isolines are dashed. $\delta_I = 0.01$, $R = 0.8$, no-slip.

collocation point of the Gauss-Lobatto grid has coordinate

$$x_1 = \frac{1}{2}\left(1 - \cos\left(\frac{\pi}{N_x - 1}\right)\right) = 0.986 \cdot 10^{-3}.$$

However, the gross features of the mode φ_{11} are very similar to the idealized basin mode (3.2) (see Pedlosky, 1987).

The most sensitive to perturbations are the spatial patterns of degenerate modes, (n, m), (m, n) corresponding to the multiple eigenvalue in the spectrum (they have the same eigenfrequencies (3.3)). Both viscosity and mean flow shift the eigenfrequencies and remove the degeneracy; however, it is the presence of the mean flow that has a crucial effect in shaping the pattern of basin modes. Recall that the advection term in (1.1) breaks symmetry of a steady solution; the corresponding term in (3.1) also breaks the symmetry of eigenfunctions. In Figure 8a we give a dramatic example of such alteration by presenting the eigenfunctions φ_{21} and φ_{12}. At the first glance there is no resemblance at all to the
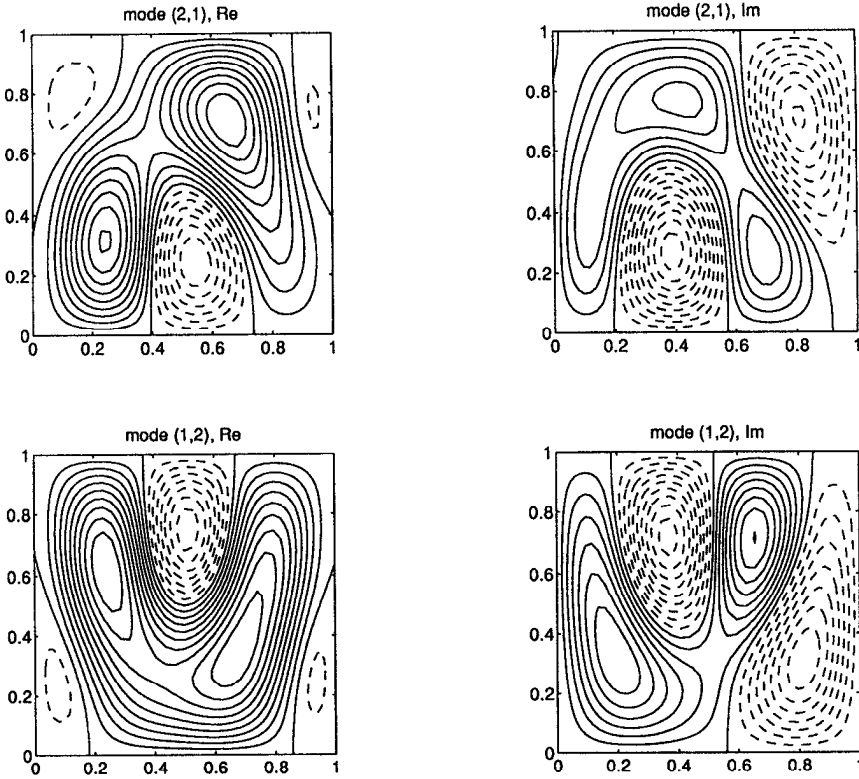
Figure 8. (b) The linear combination of the idealized Rossby basin modes $\varphi_{21}^{(0)}(x, y)$ and $\varphi_{12}^{(0)}(x, y)$, which according to (3.7) represents the perturbed degenerate pair $\varphi_{21}(x, y)$ and $\varphi_{12}(x, y)$ shown in Figure 8a.

patterns of the corresponding idealized basin modes given by (3.2). However, according to perturbation theory (to a first approximation) the perturbed eigenfunction is just a linear combination of the eigenfunctions corresponding to the unperturbed degenerate pair $\varphi_{21}^{(0)}$, $\varphi_{12}^{(0)}$ given by (3.2)

$$\varphi_{21} = A\varphi_{21}^{(0)} + B\varphi_{12}^{(0)}$$

$$\varphi_{12} = C\varphi_{21}^{(0)} + D\varphi_{12}^{(0)}.$$

(3.7)

In particular the patterns very close to those shown in Figure 8a can be produced if we put $A = 0.8073 \exp{(i\pi 1.2110)}$, $B = 0.6471 \exp{(i\pi 1.4871)}$, $C = 0.7878 \exp{(i\pi 0.0692)}$, $D = 0.9360 \exp{(i\pi 1.5040)}$. The result of such a combination is shown in Figure 8b. The given values of A, B, C and D were obtained by projecting (3.7) onto idealized basin modes and using max $(|\varphi|) = 1$ normalization of eigenfunctions. Note that (3.7) captures only the interior part of the eigenfunctions since the idealized eigenfunctions do not satisfy the dynamical boundary conditions (3.1b).

Strictly speaking, it is somewhat ambiguous to term perturbed degenerate basin modes as φ_{nm} or φ_{mn} because they are in fact some combination of the both. But since in the case with viscosity only the mode with larger x index, $n > m$, is damped more strongly and has lower frequency $(Re(\sigma))$ (see (3.5), (3.6)) this tendency usually remains even in the case with the mean flow present. Therefore, such a terminology makes sense.

When the basin is not a square, but a rectangle, the basin modes (n, m) and (m, n) are not degenerate. However, perturbations may result in incidental degeneracy, that is the eigenfrequencies of some modes may come close, then the eigenfunctions of these modes will be mixed.

Unlike the case with viscosity only, the interaction of a basin mode with the mean flow may result in either a negative or a positive shift of the imaginary part of the eigenfrequency. If the positive shift is sufficiently large, larger than the viscous damping, then the corresponding basin mode will grow. Such a resonant excitation of basin modes usually has quite an irregular character indicated in Figure 9, which shows the variation of selected eigenfrequencies for increasing Reynolds number. We observe that, as the recirculation gyre grows with the Reynolds number, some basin modes selectively happen to come in resonance with the recirculation gyre but only for a narrow range of R. For example, in Figure 9a we can see that the eigenfrequencies of the modes (4, 2), (2, 4) and (2, 2) shift very rapidly for $0.7 < R < 0.9$.

b. Resonant mode. It is the existence of a resonant mode, φ_{Res}, that causes the resonance between the recirculation gyre and the Rossby basin modes. The eigenfrequency of this mode σ_{Res} is distinct in the spectrum for $R = 0.8$ (Fig. 6b). The spatial pattern of φ_{Res} is shown in Figure 10a. Looking carefully one can distinguish a perturbation localized on the southern side of the recirculation gyre and some combination of Rossby basin modes in the basin interior. In fact, if we project φ_{Res} onto the idealized basin modes (3.2)

$$\varphi_{ResBM} = \sum_{n=1}^{M} \sum_{m=1}^{M} A_{nm} \varphi_{nm}^{(0)} \tag{3.8}$$

(it suffices to take $M = 5$), we find that the dominant amplitudes are $A_{42} = 0.1802$ $\exp{(i\pi 0.2571)}$, $A_{43} = 0.1671 \exp{(i\pi 1.3679)}$, $A_{33} = 0.1571 \exp{(i\pi 1.0237)}$, $A_{34} = 0.1477$ $\exp{(i\pi 0.2095)}$, $A_{24} = 0.1134 \exp{(i\pi 1.8632)}$, with the largest contribution from the mode $\varphi_{42}^{(0)}$. The amplitudes of the other components are smaller by at least a factor of 3.

However, φ_{ResBM} represents only the interior part. The difference, $\varphi_{Res} - \varphi_{ResBM}$ shown in Figure 10b reveals the structure of the perturbation in the recirculation gyre region, which is otherwise masked. We now clearly see a chain of positive and negative eddies travelling along the southern side of the recirculation gyre westward. (The direction of the movement can be determined by comparing the real and imaginary parts of the eigenfunction.) To mark the flank of the recirculation gyre we superimposed on Figure 10b the contour (dotted line) of potential vorticity, $q = 0.9$, of the steady solution ψ_0. It is hard to say definitely
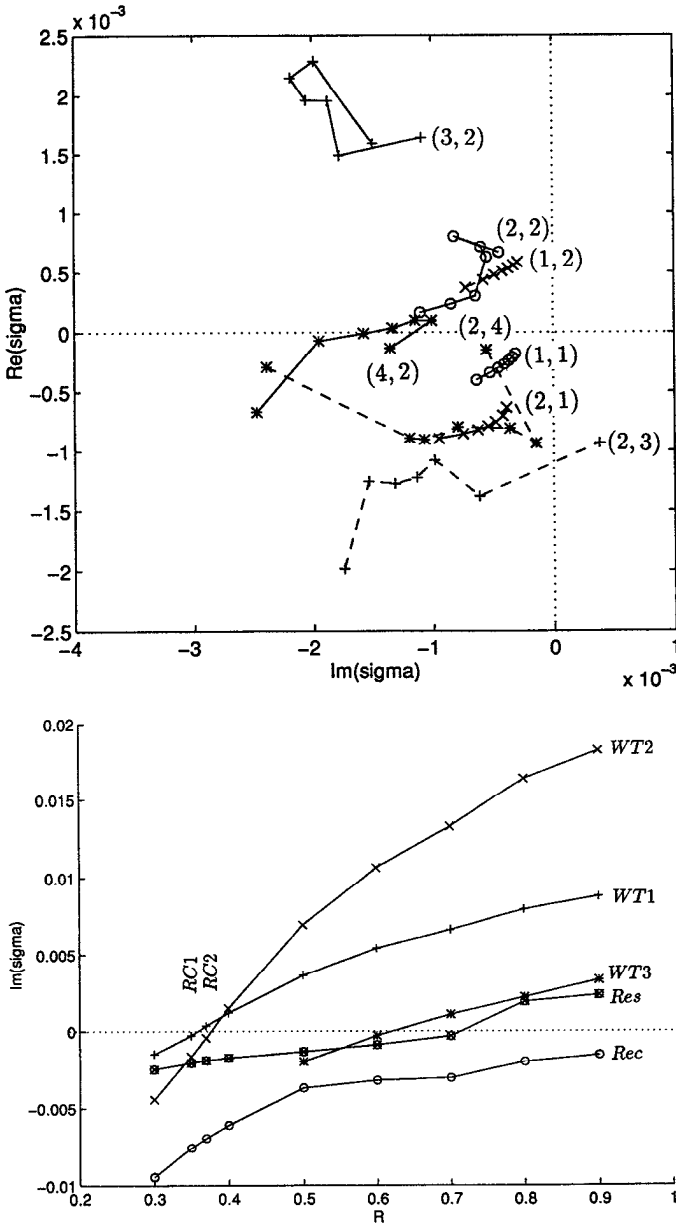
Figure 9. (a) The variation of the eigenfrequencies of some lowest Rossby basin modes with increasing Reynolds number, $\delta_I = 0.01$, no-slip, $R = 0.3, 0.4, 0.5, 0.6, 0.7, 0.8, 0.9$. The index (n, m) of each basin mode is shown next to the marker corresponding to $R = 0.9$. Combinations of marker and line styles are used to distinguish the eigenmodes. (b) The variation of the imaginary part of the eigenfrequency with the Reynolds number for some eigenmodes; $\delta_I = 0.01$, no-slip. *WT*1, *WT*2, *WT*3—the wall-trapped modes; *Res*—resonant mode; *Rec*—recirculation gyre mode. *RC*1 and *RC*2 mark the Reynolds numbers for which the modes *WT*1 and *WT*2 (respectively) start to grow. Apparently the steady solution becomes unstable for $R > R_{C1}$.
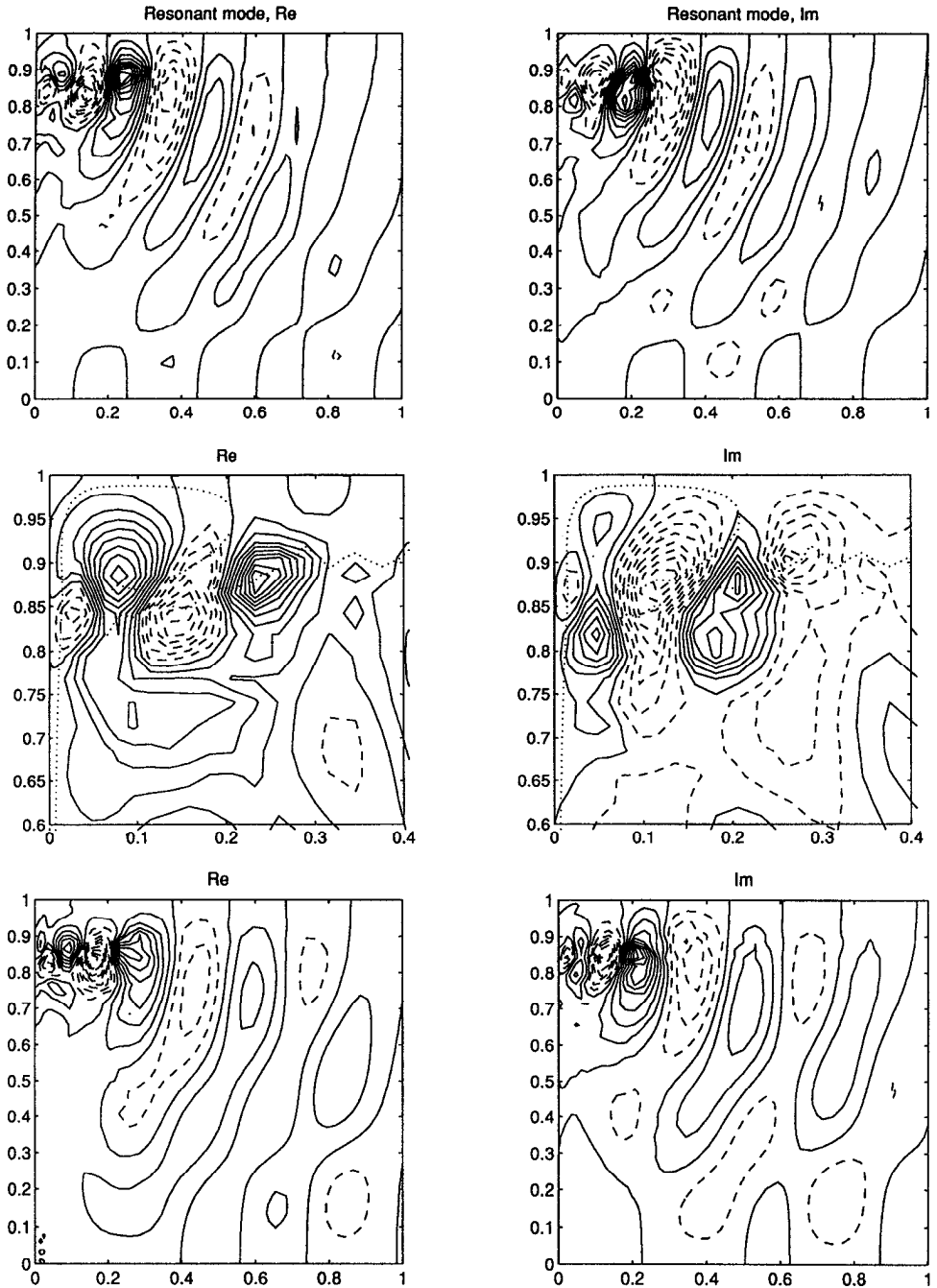
Figure 10. (a, upper row) The resonant mode $\varphi_{Res}(x, y)$ corresponding to the steady solution ψ_0, $\delta_I = 0.01$, $R = 0.8$, no-slip. $CI = 0.1$ max $(|\varphi|)$. The negative isolines are dashed. (b, middle row) The resonant mode $\varphi_{Res}(x, y)$, $R = 0.8$, with removed contribution of 25 lowest idealized Rossby modes according to (3.8) or in other words $\varphi_{Res} - \varphi_{ResBM}$. $CI = 0.1$ max $(|\varphi|)$. The negative isolines are dashed. The spatial pattern is shown on the expanded scale in the northwest corner of the basin. The dotted line shows the isoline of the potential vorticity $q = y + \delta_I^2 \nabla^2 \psi = 0.9$ of the steady solution. (c, lower row) Same as (a) but for larger Reynolds number $R = 0.9$.

what mechanism causes such instability: high gradients of vorticity in this region or deceleration of the westward flow in approaching the western boundary. Probably the former supports the wavelike oscillations while the latter makes them grow.

We term this mode "resonant" because it clearly represents a coupling between two oscillatory processes: eddies on the southern flank of the recirculation gyre and certain basin modes of Rossby waves. The resonant mode is distinguished by a peculiar type of eigenfunction having large amplitude perturbation localized near the recirculation gyre and a tail of smaller amplitude Rossby waves extending to, and decaying in, the basin interior. Such a pattern suggests an interpretation in terms of wave propagation: the instability extracts energy from the mean flow and radiates it into the interior with a southeastward group velocity associated with short Rossby waves.

As the Reynolds number increases the recirculation gyre grows, so does the velocity of the flow on its southern side and therefore the real part of the eigenfrequency of the resonant mode gets higher. For $R = 0.9$ (note the last open circle adjacent to σ_{Res} in Fig. 6b) $Re(\sigma_{Res})$ comes close to the eigenfrequencies of the basin modes $(3, 2)$ and $(2, 3)$. As a consequence these modes come into resonance with the eddies on the southern flank of the recirculation gyre. The pattern of φ_{Res} for $R = 0.9$ is shown in Figure 10c. We see that the spatial scale in the interior has become larger than in Figure 10a. The projection onto the idealized basin modes reveals that the contribution in the interior is indeed mostly from $\varphi_{32}^{(0)}$ and $\varphi_{23}^{(0)}$: $A_{32} = 0.2176 \exp{(i\pi 0.5864)}$, $A_{23} = 0.1859 \exp{(i\pi 1.3353)}$, $A_{33} = 0.1024$ $\exp{(i\pi 1.7687)}$, $A_{42} = 0.0934 \exp{(i\pi 0.8417)}$, $A_{24} = 0.0439 \exp{(i\pi 0.5718)}$; the rest of the amplitudes are much smaller. It is important to note that the resonant eigenmode is distinct from the modes $(3, 2)$ and $(2, 3)$ and other basin modes. In other words, apart from σ_{Res} there are eigenfrequencies σ_{32} and σ_{23} present in the spectrum.

Thus as the recirculation gyre becomes prominent there appear favorable conditions for instability on its southern flank. This instability in turn drives the Rossby basin modes which happen to have nearby frequencies and similar spatial scales. Due to the resonance the spatial patterns of the instability and Rossby modes become mixed. The large amplitude of φ_{Res} in the interior of the basin implies efficient energy transfer from the instability to the Rossby waves.

As seen in Figure 6, the lowest basin modes with small n, m are very distinct in the eigenspectrum. As the numbers n, m increase the density of eigenfrequencies on the plot also increases. Irregular shifts in eigenfrequencies due to interaction with the mean flow cause the eigenfunctions of many modes to become mixed. Therefore, for large n, m it becomes almost impossible to recognize in the eigenfunction its idealized precursor. Fortunately, this is not really needed. Higher modes have smaller spatial scales and thus decay more rapidly.

c. *Recirculation gyre modes*. Though not the most conspicuous at a first glance, a mode with zero real part of the eigenfrequency, $Re(\sigma_{Rec}) = 0$, (nonoscillatory mode) lying closest to the origin (Fig. 6) is of great importance. As discussed in IS, this mode is responsible for
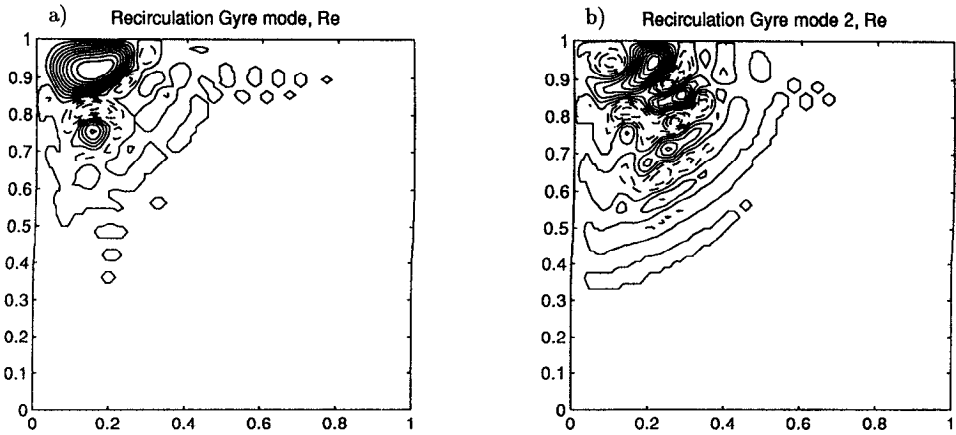
Figure 11. (a) The recirculation gyre mode $\varphi_{Rec}(x, y)$ and (b) the recirculation gyre mode 2, $\varphi_{Rec2}(x, y)$, corresponding to the steady solution ψ_0, $\delta_I = 0.01$, $R = 0.8$, no-slip. These modes are nonoscillatory, $Re(\sigma) = 0$, their imaginary parts are identically zero; therefore, only the real part is plotted. $CI = 0.1$ max $(|\varphi|)$. The negative isolines are dashed.

the existence of multiple solutions in the problem. When we consider a steady solution such that we approach a nose point the eigenfrequency $(Im(\sigma_{Rec}))$ of this mode tends to zero. At the low nose point $R = R_L$ (or at the high nose point $R = R_H$) the eigenfrequency of this mode vanishes exactly, $\sigma_{Rec} = 0$.

According to the Fredholm theorem for linear operators, the existence of a zero eigenvalue means that the solution of the problem is not unique. The same conclusions can be drawn for a zero eigenvalue of the Frèchet derivative (3.1) for our nonlinear problem. In application to our problem this translates into the statement that the family of functions

$$\psi_{0L} + \sqrt{\epsilon}\, \varphi_{RecL} \tag{3.9}$$

with one parameter $\sqrt{\epsilon}$ represents (to a linear approximation) steady solutions in the vicinity of the low nose point, where ψ_{0L} is the steady solution at the very low nose point and φ_{RecL} is the corresponding recirculation gyre eigenfunction. In other words (3.9) corresponds to the vertical portion of $Q(R)$ curve near R_L.

The pattern of the eigenfunction φ_{Rec} (Fig. 11a) for the steady state ψ_0 belonging to the low branch (Fig. 5b) resembles the recirculation gyre, therefore we call this eigenmode the recirculation mode, φ_{Rec}. This mode reflects the change of recirculation gyre intensity. Thus from the physical point of view the existence of the low, middle and high branches of steady solutions is connected with the formation of the recirculation gyre in the northwest corner of the basin. As the steady solution ψ_0 changes, when parameters vary, the spatial pattern of the recirculation mode also changes. When one moves from the low to high branch the recirculation gyre grows to fill the whole basin, so does the pattern of φ_{Rec}.

The imaginary part of eigenfrequency of this mode is negative on the low branch, $Im(\sigma_{Rec}) < 0$, positive on the middle, $Im(\sigma_{Rec}) > 0$, and again negative on the high branch,
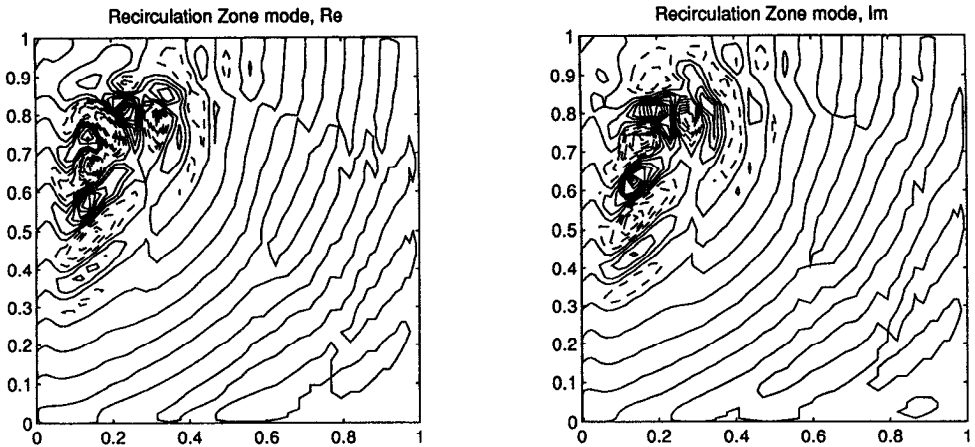
Figure 12. The recirculation zone mode $\varphi_{RZ}(x, y)$ corresponding to the steady solution ψ_0, $\delta_I = 0.01$, $R = 0.8$, no-slip. $CI = 0.1$ max ($|\varphi|$). The negative isolines are dashed.

$Im(\sigma_{Rec}) < 0$. Thus the middle branch is unstable. Such a behavior of one eigenmode is in accord with the most generic bifurcation A_3 (Whitney tuck) of a two parameter (δ_M, δ_I) dynamical system (Arnol'd, 1984). The instability of the middle branch with respect to φ_{Rec} means that starting from the middle branch as an initial condition the time-dependent solution would tend either to the high or to the low branch depending on the sign of the initial disturbance. (Bear in mind that this behavior is with respect to the single mode, σ_{Rec}. *Other* modes can (and do) destabilize both upper and lower branches.)

We note that in the eigenspectrum (Fig. 6) there is a sequence of eigenfrequencies with $Re(\sigma) = 0$ corresponding to nonoscillatory modes. Some of them are also associated with the existence of the recirculation gyre. For example, another nonoscillatory mode (σ_{Rec2}), next to the σ_{Rec} on the left, represents a next spatial harmonic. The pattern of the eigenfunction φ_{Rec2} (Fig. 11b) resembles the recirculation gyre divided in halves. It can be interpreted as a change in the eastward extent of the recirculation gyre. Since this mode has smaller spatial scales it decays faster.

d. Recirculation zone modes. There are also a number of eigenfrequencies in the spectrum (Fig. 6b) which lie distinctly outside the envelope of basin modes and have lower frequencies than the wall-trapped modes (discussed further below). We term the corresponding eigenmodes collectively as recirculation zone modes. Their spatial patterns do not allow simple interpretation of the physical mechanisms responsible for their emergence (e.g. Fig. 12). However, it is apparent that they are related to the nonuniform distribution of potential vorticity in the recirculation zone.

e. Wall-trapped modes. The nonuniform distribution of vorticity in the western boundary layer gives rise to another type of wave motion—vorticity waves. These waves are similar
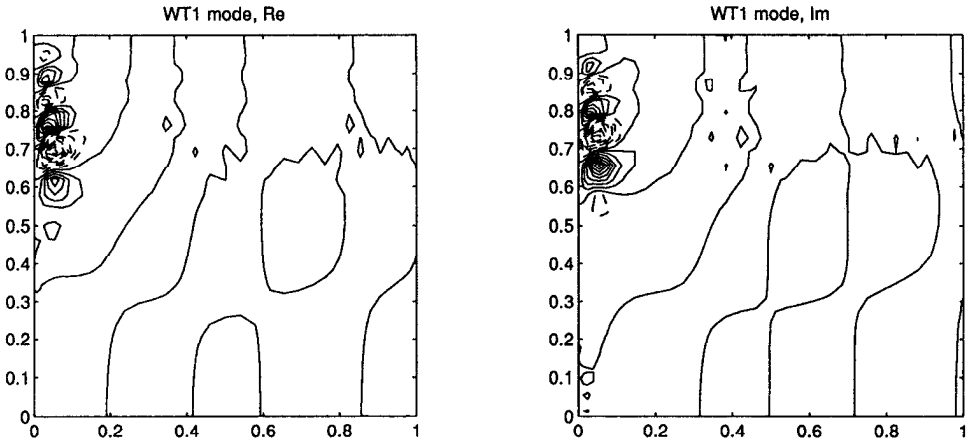
WT1 mode, Re

WT1 mode, Im

Figure 13. The wall-trapped mode $\varphi_{WT1}(x, y)$ corresponding to the steady solution ψ_0, $\delta_I = 0.01$, $R = 0.4$, no-slip. This mode starts to grow for $R > R_{C1} = 0.353$. $CI = 0.1$ max $(|\varphi|)$. The negative isolines are dashed.

to the waves described by the Orr-Sommerfeld equation for the parallel flow. Their linear combinations constitute wall-trapped modes. Their eigenfunctions are confined to the region of the western boundary current and decay offshore.

In Figure 6 eigenfrequencies of the wall-trapped modes lie distinctly outside the envelope of the Rossby modes. As an example, we consider two marked *WT1* and *WT2* on the plots. As the Reynolds number increases starting from zero the imaginary part of eigenfrequency of the mode *WT1* is the first to cross zero at $R_{C1} = 0.353$ (Fig. 9b). For $R > R_{C1}$ *Im* (σ_{WT1}) of this mode becomes positive and therefore the steady solution becomes unstable. The mode *WT2* begins to grow for $R > R_{C2} = 0.377$. For $R = 0.4$ in Fig. 6a there are two growing modes: *WT1* and *WT2*. The corresponding eigenfunctions are shown in Figures 13, 14. As we see, the wall-trapped mode *WT1* is just a higher spatial harmonic in y as compared to *WT2*. For $R = 0.8$ the growth rate of *WT1* and *WT2* increase significantly; the real part of the eigenfrequencies also differ due to the change of the basic flow ψ_0, mostly because of the recirculation gyre affecting the return current in the northern part of the western boundary layer.

The wall-trapped mode *WT3* starts to grow at $R = 0.62$ (Fig. 9b). The spatial pattern of this mode is not truly confined to the western boundary, but it is localized in the region of the return flow adjacent to the main north-going western boundary current.

According to the dispersion relation the maximum frequency σ_{max} of barotropic Rossby waves with a given latitudinal wavenumber l is attained for the zonal wavenumber $k = -l$, $\sigma_{max} = 1/(2l)$. Taking $l = 2\pi/0.16$, corresponding to the oscillatory pattern near the western boundary of the wall-trapped mode *WT2* for $R = 0.8$ (Fig. 14), gives $\sigma_{max} = 0.0127$ which is significantly smaller than the eigenfrequency $Re(\sigma_{WT2}) = 0.052$. Thus, as earlier appreciated by Ierley and Young (1991) in a simpler parallel flow model of the western boundary current, oscillations in the boundary layer cannot radiate Rossby waves into the
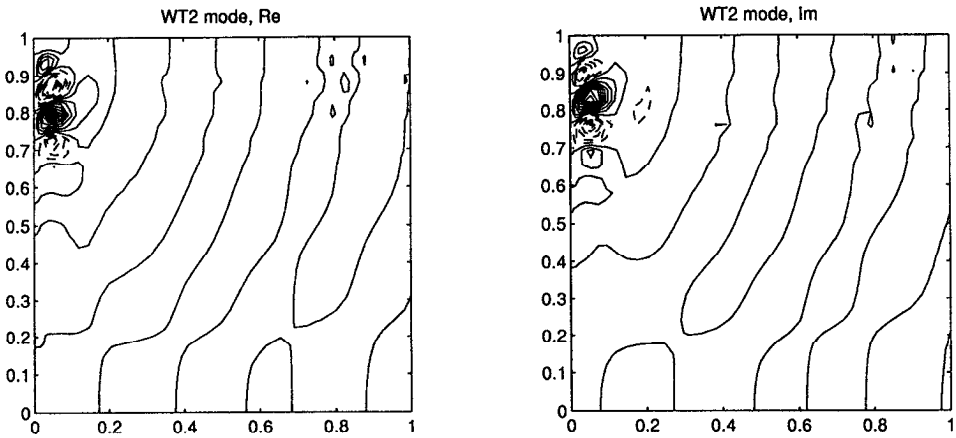
Figure 14. The wall-trapped mode $\varphi_{WT2}(x, y)$ corresponding to the steady solution ψ_0, $\delta_I = 0.01$, $R = 0.4$, no-slip. This mode starts to grow for $R > R_{C2} = 0.377$. $CI = 0.1$ max ($|\varphi|$). The negative isolines are dashed.

interior and as a result the eigenmode becomes "wall-trapped." Note that the eigenfrequency of $WT3$ is lower and closer to the corresponding σ_{max}, therefore the eigenfunction of $WT3$ decays more slowly offshore.

The pattern of the wall-trapped eigenfunctions resembles the eddies in the western boundary layer observed in many time-stepping numerical experiments (Bryan, 1963; Godfrey, 1973, KSPB, SKP). We shall return to more detailed comparison in the next section.

To conclude this section we briefly discuss stability of the middle and high branches of steady solutions. Following the low branch, as the Reynolds number increases, approaching the low nose value R_L, there appear more and more growing eigenmodes. Following the middle branch yet more eigenmodes are destabilized despite the slight decrease in Reynolds number. This is due to the dramatic increase of the amplitude of recirculation. (Some of this effect may be transient, however. That is, certain eigenmodes may indeed turn back and become decaying, especially in approaching the high nose point.) On the high branch there also exist many growing eigenmodes which render the high branch solution unstable for all R examined.

It is worth pointing out that as the structure of the steady solution changes so does the structure of the eigenfunctions. The beta-effect is dominant on the lower branch while on the high branch advection is the dominant factor. For example, the lowest Rossby wave basin mode of the low branch progressively deforms until, far along the high branch, one identifies it as the lowest Lamb mode of a uniformly rotating gyre.

It is interesting to note, as commented in IS, that in the slip case the high branch solution ultimately becomes stable for large R. As the Reynolds number increases from R_H all the growing modes eventually turn back to the stable region $Im(\sigma) < 0$. Stabilization of the high branch can be attributed to the structural change of the solution which becomes

simpler: both the stream function and vorticity tend to the lowest Helmholtz eigenfunction of the basin $\sin(\pi x)\sin(\pi y)$ (see IS). Evidently no such simple behavior exists for the no-slip case.

4. Comparison with the time-dependent solution

The time-stepping experiments with the same problem (no-slip case, $\delta_I = 0.01$, varying R) were carried out in KSPB and SKP using a finite-difference method. It was observed that for a Reynolds number smaller than the critical value $R_C = 0.38$ the time-dependent solution approaches a steady state which is essentially the same as ψ_0 obtained in this work using the spectral method. For $R > R_C = 0.38$ the time-dependent solution does not stabilize as time proceeds; eddies were observed forming in the northern part of the western boundary current.

The estimate for the critical Reynolds number R_C were obtained based on the dependence of the kinetic energy of the eddies on R. This estimate is in a good agreement with the results of linear stability analysis, which indicates that the first wall-trapped mode (WT1) starts to grow at a Reynolds number of $R_{C1} = 0.353$ and the second wall-trapped mode (WT2) at $R_{C2} = 0.377$. Moreover, the Fourier spectra of the time records of the stream function in the western boundary layer in the time-dependent problem for the Reynolds number just above the critical value show the existence of two primary peaks. For $R = 0.4$ we have $\sigma_1 = 0.046$, $\sigma_2 = 0.031$ (Fig. 7 in KSPB). These σ agree well with the eigenfrequencies of the wall-trapped modes of the steady (unstable) solution for the same $R = 0.4$: $Re(\sigma_{WT1}) = 0.046$ and $Re(\sigma_{WT2}) = 0.033$. Most convincing, however, is the fact that the pattern of the second wall-trapped mode is very similar to the pattern of the eddies in the western boundary current. These results evidence that in the vicinity of R_C the sum ψ_0 plus a linear combination of φ_{WT1} and φ_{WT2} can satisfactorily approximate the time-dependent solution as long as the amplitudes of perturbations are small.

Beyond the first instability, $R > R_C$, the eddies and other pulsations produce Reynolds stresses which modify the dynamical balance. Therefore a time-averaged circulation no longer matches the steady (unstable) solution. Figure 15 compares the maximum value of the stream function $Q(\psi_0)$ of the steady solution (solid line) with the same characteristic of the time-averaged solution $Q(\bar{\psi})$ from SKP (dashed line). We see that $Q(\psi_0)$ continuously increases with R and tends to the low nose value at $R = R_L = 1.6$ where the low branch of the curve folds back onto the middle branch. On the other hand, $Q(\bar{\psi})$ begins to deviate from $Q(\psi_0)$ for $R > R_C$ and remains approximately constant up to $R = R_L$. Then the recirculation gyre in the time-averaged solution begins to grow rapidly and $Q(\bar{\psi})$ increases for $R > R_L$.

It was argued in KSPB and SKP that the observed saturation of the time-averaged solution in the range of Reynolds number $R_C < R < R_L$ is due to the enhanced diffusion of positive vorticity from the western boundary due to the eddies. The saturation is also clearly seen in the energy partitioning (Fig. 11 from SKP); the total kinetic energy of the time-averaged circulation E_m closely follows the kinetic energy of the linear (Munk)
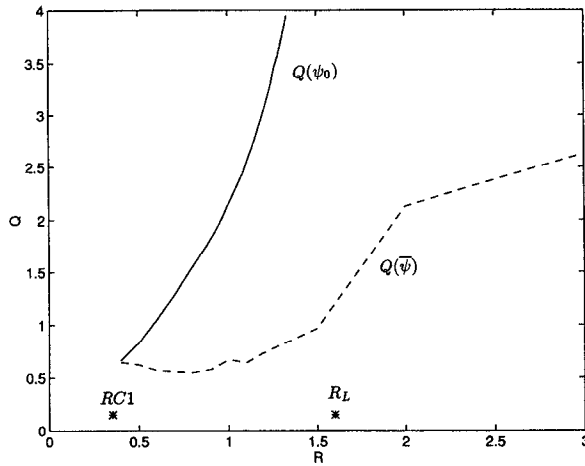
Figure 15. The comparison of the maximum of the stream function within the recirculation gyre for the steady (but unstable) solution ψ_0 (solid) and for the time-averaged solution $\bar{\psi}$ (dashed), $\delta_I = 0.01$, no-slip. $RC1$ marks the Reynolds number for which the wall-trapped mode $WT1$ starts to grow (the first instability). R_L marks the Reynolds number corresponding to the low nose point.

solution E_{Munk} for the same viscosity; only for $R > R_L$ when the recirculation gyre increases in size does E_m begin to deviate significantly from E_{Munk}.

The breakdown of steady solutions ψ_0 at R_L and the rapid growth of the recirculation gyre in the time-averaged solution $\bar{\psi}$, which starts around R_L, have a common cause—splitting of the western boundary current into an inertial part and a viscous sublayer. In the steady case the amount of negative vorticity carried to the north by the inertial part of the boundary current becomes exceedingly large so that viscous forces fail to compensate it. In the time-dependent case the efficiency of eddies in enhancing the flux of positive vorticity from the western boundary becomes limited; they no longer can easily extract positive vorticity from the viscous sublayer. Both effects should happen at similar Reynolds numbers, namely, when the splitting of the inertial-viscous boundary current becomes prominent.

If we compare the properties of eddies derived from the fully nonlinear time-dependent problem with those predicted by linear eigenanalysis of the steady (unstable) solution for R greater than but not very close to R_C we get only qualitative agreement. For example, for $R = 0.8$ the eddies in the time-dependent solution have a dominant frequency $\sigma_e = 0.0234$. The eigenspectrum corresponding to the steady solution for $R = 0.8$ (Fig. 6b), on the other hand, has the primary wall-trapped mode $WT2$ with $Re(\sigma) = 0.052$ and its growth rate is significant. Figure 16a shows the eddies on the expanded scale in the time-dependent experiment with $R = 0.8$ ($R08M$ in KSPB and SKP); the departure of the instantaneous stream function at time $t = 10000$ from the time-averaged solution is plotted. Figure 16b shows the pattern of the eigen stream function of the wall-trapped mode $WT2$ in the eigenproblem linearized about the steady (unstable) solution for $R = 0.8$. We see that the
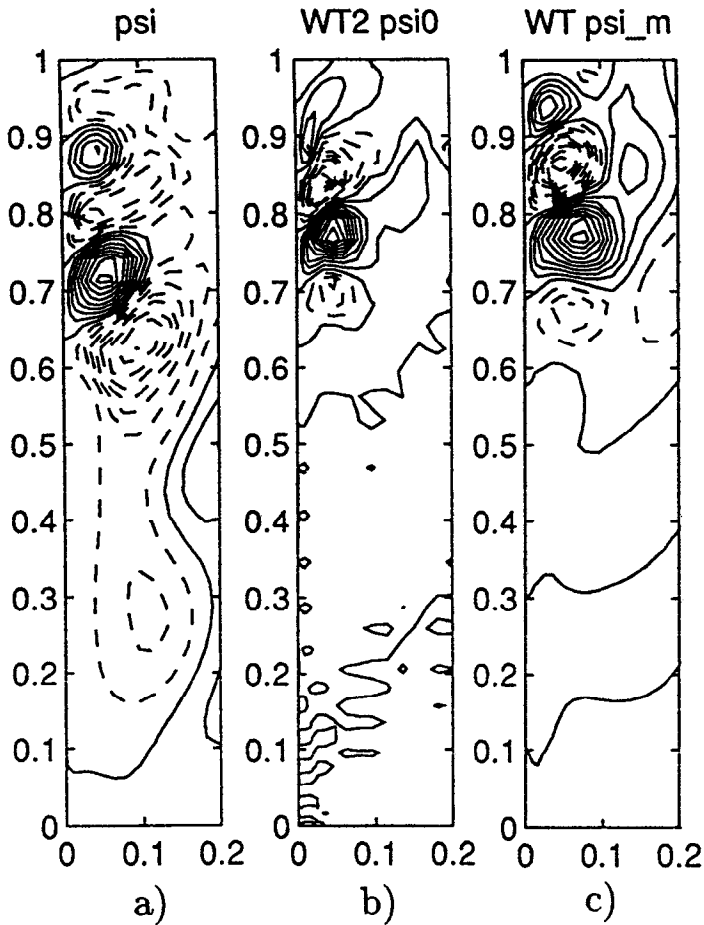
Figure 16. The comparison of the spatial patterns of the eddies in the western boundary current with spatial patterns of the wall-trapped eigenmodes. $\delta_I = 0.01$, $R = 0.8$, no-slip. (a) The departure of the instantaneous stream function at $t = 10000$ from the time-averaged stream function, $\psi(x, y, t = 10000) - \bar{\psi}(x, y)$ (the results of the time stepping problem (KSPB, SKP)). $CI = 0.1$. (b) The real part of the wall-trapped mode *WT2* corresponding to the steady solution ψ_0. $CI = 0.1$ max $(|\varphi|)$. (c) The real part of the wall-trapped mode *WT* corresponding to the time-averaged solution ψ. $CI = 0.1$ max $(|\varphi|)$. The absolute value of the eigenfunction of the linearized problem is irrelevant. The negative isolines are dashed.

size of the eddies in Figure 16a is noticeably larger than the corresponding scale in Figure 16b.

This is natural. We shouldn't expect too much agreement merely because the time-averaged solution (Fig. 17a) and steady (unstable) solution (Fig. 5b) are quite different for such a Reynolds number; the latter has a noticeable recirculation gyre while the former does not. The results of the linear eigenanalysis, strictly speaking, are applicable only when
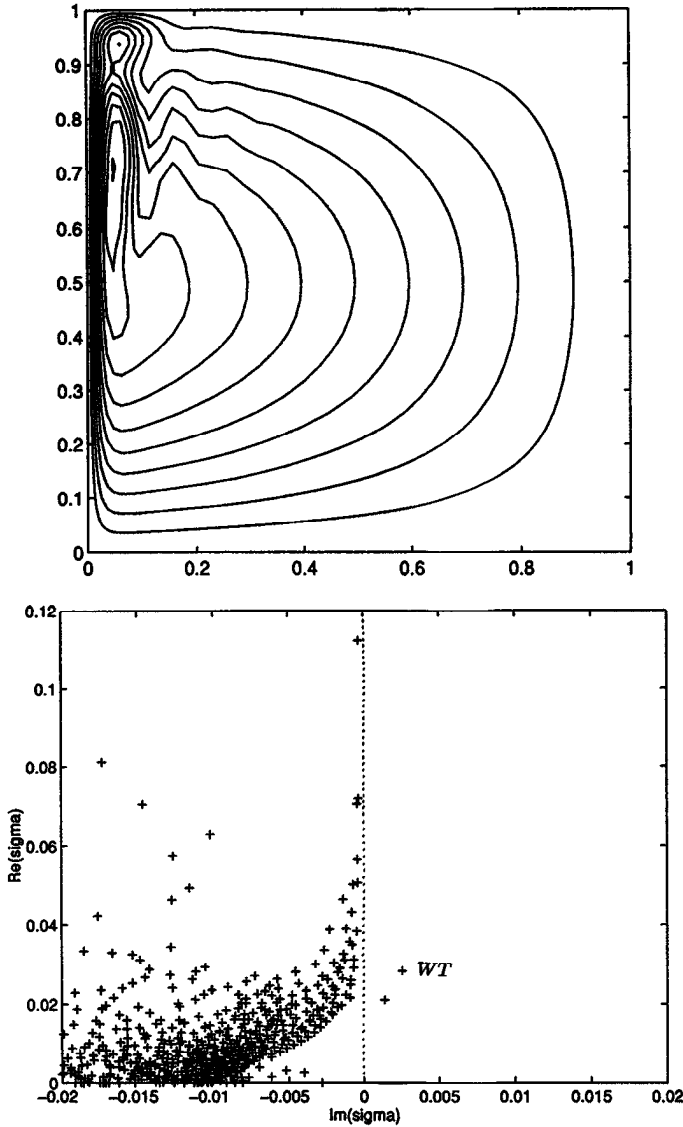
Figure 17. (a) The stream function $\overline{\psi}(x, y)$ of the time-averaged solution used in calculation of the eigenspectrum. $\delta_I = 0.01$, $R = 0.8$, no-slip. $CI = 0.1$. Compare this with the steady (unstable) solution shown in Figure 5b. (b) The eigenspectrum of the time-averaged solution $\overline{\psi}$. The eigenfrequency of the wall-trapped mode shown in Figure 16c is marked by WT.

the amplitudes of perturbations are small. The time-dependent solution spends most of the time bouncing around the time-averaged solution, and as the time-stepping numerical experiments show, never comes close to the steady (unstable) one. In other words the intensity of the recirculation gyre in the time-dependent solution is always considerably smaller than in the steady solution ψ_0.

As an alternative we can explore the linear stability of the time-averaged solution $\bar{\psi}$ (Fig. 17a); in other words we put $\bar{\psi}$ instead of ψ_0 as a basic flow in (3.1). Though not formally justified (unless, rather artificially, we think of Reynolds stress as an externally imposed force), this procedure does have an intuitive appeal as a heuristic way to explore the stabilization of the mean profile. Thus the growth rate for a mode of the steady solution that induces a supercritical Hopf bifurcation, for example, should have an analogous, but reduced, value for an associated mode of the time-dependent problem, consistent with the idea of saturation determined by a Landau equation.

The resulting eigenspectrum is shown in Figure 17b. There are only two marginally unstable modes. The eigenfrequency of the wall-trapped mode $\sigma_{WT} = 0.028$ of the time-averaged field agrees better with the frequency of eddy formation $\sigma_e = 0.0234$. Moreover, the pattern of the corresponding eigenfunction shown in Figure 16c has a scale much closer to the size of the eddies in Figure 16a.

Thus we conclude that for the analysis of time variability in the fully nonlinear time-dependent problem, one obtains better agreement by using the eigenmodes of the time-averaged solution. While such an approximation can only be rigorously justified for a mean field expansion with appropriately small interaction terms, there is considerable intuitive appeal to the idea that turbulent disturbances continually drive the flow back toward marginality. One common atmospheric idealization of this sort is the assumption that the atmosphere relaxes back to the neutral adiabat. For fully-developed turbulent flow in a channel, the mean profile goes well past marginal, it is superstable with respect to linear two-dimensional "Orr-Sommerfeld" disturbances. (The quotes are used to reinforce the purely formal correspondence in the form of the equation to the classic O-S problem.) However, recognizing the characteristic role of subcritical three-dimensional disturbances in shearing flow, one can find an adjacent problem in which, with the postulate of an underlying two-dimensional traveling O-S wave of moderate amplitude, the one-dimensional mean is rendered just marginal with respect to three-dimensional waves.

Finally, we can answer the question why the eddies are observed in the time-dependent problem with no-slip condition at the western boundary and absent in the problem with the slip boundary condition (see KSPB, SKP and also Böning, 1986). Recall that one-dimensional stability analysis of the parallel flow with the profile as in the Munk boundary layer suggests that the slip case should be the more unstable (Ierley and Young, 1991). In the one-dimensional problem one should distinguish between *convected instability* and *absolute* or *nonconvected instability* (Drazin and Reid, 1981). If the group velocity c_g of disturbance is sufficiently large (as apparently in the slip case) then the perturbation (though convectively unstable) will move away from the unstable region and a solution as a whole will be stable. On the contrary, if the group velocity is relatively small (as shown in Cessi and Ierley, 1993), then the perturbation will efficiently grow and result in instability of the flow.

In the two-dimensional stability problem there is no such dilemma. If the imaginary part of the eigenfrequency is positive then the mode is growing, and the solution is truly unstable. This is so because an eigenmode *does not* carry energy from one place to another,

the group velocity of an eigenmode in a bounded domain is zero by definition; it is actually a linear combination of the waves carrying energy in opposite directions so that the net flux is zero. In fact in the slip case (same $\delta_I = 0.01$) it is the resonant mode that starts to grow first at $R = 0.37$. Since in the slip case the size of the recirculation gyre is larger, the resonant mode is mixed with the basin modes (3, 2) and (2, 3). However, the eigenproblem (3.1) with slip boundary conditions also has the wall-trapped mode corresponding to eddies in the western boundary layer, but this mode starts to grow for larger Reynolds number $R > R_{WTSlip} = 0.515$. The absence of eddies in the time-dependent problem with slip boundary conditions can apparently be attributed to the fact that at R_{WTSlip} the time variability is already dominated by the basin mode which starts to grow first.

5. Conclusions

The classical barotropic model of the wind-driven ocean circulation in the subtropical gyre was considered. The nondimensional vorticity equation (1.1) was analyzed in the square domain $0 \le x, y \le 1$. The impermeability and no-slip conditions (1.2a) were specified at the coasts ($x = 0; 1$) and the impermeability and slip conditions (1.2b) at the fluid boundaries ($y = 0; 1$). The solutions of the problem (1.1), (1.2) are governed by two nondimensional parameters δ_I and δ_M: $\delta_I =$ (inertial boundary layer width)/L, $\delta_M =$ (viscous boundary layer width)/L, where L is the scale of the domain of integration. Sometimes it appeared convenient to use the Reynolds number R, defined as the cube of the ratio of δ_I and δ_M, instead of δ_I or δ_M. We concentrated on the analysis of the solutions of the problem for geophysically meaningful values of the parameters δ_I, δ_M ($0 \le \delta_I, \delta_M \le 0.1$).

First, the existence and the structure of steady solutions of the problem (1.1), (1.2) were analyzed. It was found that for every δ_I, δ_M there is at least one steady solution. The structure of these solutions can be of three types: boundary-layer, recirculation and basin-filling-gyre. It was shown that a certain subdomain of the parameters δ_I, δ_M exists for which the problem (1.1), (1.2) has three steady solutions of indicated types. In a three-dimensional space a surface given by $Q = Q(\delta_I, \delta_M)$, where Q is the maximum value of the stream function, forms the so-called Whitney tuck. Projecting this surface onto the plane δ_I, δ_M gives the wedge-shaped region where three steady solutions coexist. The tip of this wedge is located at $\delta_I = 0.05637$, $\delta_M = 0.04223$. The corresponding Reynolds number $R = 2.378$ and maximum value of the stream function $Q = 2.90$. At this point all three solutions coalesce in a cusp singularity. There are some indications that possibly several Whitney tucks exist for larger values of δ_I, δ_M.

The detailed comparison with the problem with the slip boundary conditions at the coasts is presented. The main conclusion is that in the vicinity of the main Whitney tucks (for $R < 50$) the general character of the steady solutions of the problem with no-slip and slip boundary conditions at the coasts is the same, although the location of the tucks on δ_I, δ_M plane differs (the no-slip cusp and fold pattern is shifted to a larger R as compared to the slip ones). In other words, the topological structure of the steady solution space is robust with respect to boundary conditions at the coasts.

It is helpful to present the above mentioned results in a slightly different way. Consider

the case of fixed $\delta_I = 0.01$ and varying R that is relevant for the study of the wind-driven North Atlantic subtropical gyre. For this case the maximum value of the stream function Q as a function of R consists of three branches (forming the S-shaped curve): low, middle, and high. The low branch solutions are basically of boundary layer type (especially for small R). At $R = R_L = 1.6$ the low branch turns back, forming a middle branch. The middle-branch solutions are characterized by a strong recirculation gyre. The middle branch turns into the upper branch at $R = R_H$ (around 0.6 for $\delta_I = 0.01$). The upper branch solutions are of basin-filling-gyre type and have high amplitudes. Thus the function $Q = Q(R)$ is a three-valued function for some range of R.

The steady solution of the boundary-layer type ceases to exist when R exceeds a critical value R_L. The only steady solution for such R is of basin-filling-gyre type (upper branch), but such a solution has unrealistically high velocities. Thus, for $\delta_I = 0.01$ and $R > R_L$ the solution of the problem (1.1), (1.2) with, for example, zero initial condition (or with a reasonable amplitude of the initial stream function) will likely not stabilize with time. (It was proven also that the steady solution for $R > R_L$ is unstable.) It is difficult to characterize the evolution of such solutions for large time which is why this question remains open, though recent complementary work by Berloff and Meacham (private communication) on a closely related problem suggests the ubiquity of strange attractors.

Second, the stability of the steady solutions of the problem of (1.1), (1.2) was investigated. We restricted ourselves to traditional linear mode analysis. In such an approach the time dependent problem for perturbations of the basic flow is reduced to a spectral problem for determining the possible eigenfrequencies of the eigenmodes and the structure of the eigenmodes themselves. It was shown that the low branch solutions are stable for $R < R_C$ ($R_C = 0.353$ for $\delta_I = 0.01$); the middle and high branch solutions are unstable. (In the problem with slip boundary conditions the high branch solutions are stable for large R.) The following types of the eigenmodes were identified: (1) basin Rossby modes, which are just modified (by friction and main flow) Rossby wave modes; (2) a resonant mode representing a coupling of eddies on the southern flank of the recirculation gyre and certain basin modes of Rossby waves; (3) recirculation gyre modes characterized by zero real part of the corresponding eigenfrequencies (nonoscillatory modes); (4) recirculation zone modes related to the nonuniform distribution of potential vorticity in the recirculation zone; and (5) wall-trapped modes confined to the region of the western boundary current and decaying offshore. As the Reynolds number increases (for fixed δ_I) the wall-trapped modes start to grow first, determining a first critical Reynolds number, R_C. The resonant mode starts to grow at a larger Reynolds number providing a strong coupling between the mean circulation and Rossby basin modes. The recirculation gyre modes play an important role in causing the instability of the middle branch solutions, which have a prominent recirculation gyre.

The eigenmode analysis is illuminating in the study of the evolution of the model. The spatial structure of numerical solutions of the nonlinear problem bears quantitative resemblance to the patterns of eigenmodes, especially if the Reynolds number does not

significantly exceed the critical value R_C. Using different methods Meacham and Berloff (1996) found a spatial structure of the most rapidly growing perturbation which agrees with the pattern of our wall-trapped eigenmodes. At the same time we note that for larger R (not very close to the critical value R_C) we obtain only a qualitative agreement between flow patterns derived from the nonlinear time-dependent problem and that predicted by linear eigenanalysis of the steady (unstable) solution. For example, the intensity of the recirculation gyre in the time-dependent solution is always considerably smaller than in the steady solution. Finally, for the analysis of time variability in the nonlinear time-dependent problem, it is more useful to consider the eigenmodes of the time-averaged solution considered as the basic flow in the stability analysis. The linear stability analysis explains also why the evolution of the model with slip coastal boundary conditions is different from the no-slip case (there are no eddies observed in the western boundary layer contrary to the no-slip case).

We have discussed two mechanisms for the excitation of (barotropic) Rossby waves in the problem considered: wall-trapped disturbances and disturbances on the southern side of the recirculation gyre. We believe that the former is probably not an efficient means of coupling since, according to the analysis of a simplified one-dimensional boundary layer problem (Ierley and Young, 1991) the wall-trapped disturbances do not radiate. In the well-known numerical (two-layer QG) simulations by Holland (1978) barotropic basin modes are very strong. These are strikingly reminiscent of the resonant mode presented here, suggesting that further analysis could prove quite edifying. This may be the essential dynamical link underlying the intriguing time series analysis of Miller *et al.* (1986).

Numerical integration of the nonlinear model indicates that both the spatial extent and strength of the recirculation continue to increase for larger R (SKP). In IS it was suggested that the circulation does not, nor should it, saturate in the limit of vanishing lateral viscosity. The role of instability is simply to retard the rate of growth. Barotropic instability alone, we argue, is insufficient to retard the increase in recirculation beyond realistic values. Baroclinic instability and internal gravity waves are obvious candidates for future investigation.

In conclusion we would like to stress the following point. From the mathematical standpoint (1.1) is a differential equation with the small parameters δ_I^2 and δ_M^3 appearing as coefficients of the highest derivative terms. Typically, a boundary-layer structure is characteristic of the solutions of such an equation. Relative to the solution of the low-order (limiting) equation, these boundary layers either appear adjacent to the boundaries of the domain, where they act to remove residuals in satisfying (higher order) boundary conditions, or else manifest themselves as internal boundary layers, where they heal discontinuities in the marriage of low order solutions proceeding independently from each boundary. The formation of the recirculation gyre with x- and y-scales of the same order for certain relations between the small parameters (or some Reynolds numbers) is an anomaly that runs counter to this expectation. The gyre destroys the boundary-layer structure of the moderately viscous, steady, solution and requires for its existence that high-order terms to

be taken into account (within the gyre $\delta_I^2 J(\psi, \Delta\psi) \sim \partial\psi/\partial x$). (Though the appearance of strong gradients of vorticity at the margins of the recirculation gyre constitutes the reestablishment, if you will, of an internal boundary layer.) Physically the formation of the gyre has previously been explained (IS, KSPB, SKP), however the *mathematical* necessity of the gyre does not follow from traditional *a priori* arguments such as those of the classical boundary layer theory noted above.

On the generality of our findings, it is pertinent to note that in a multilayer problem the solutions analyzed correspond to the solution describing the uppermost layer exposed to the wind forcing with the lower layers at rest. That is why we expect that our results are applicable not only to the barotropic problem broached here but to the steady solution of the baroclinic case as well.

REFERENCES

Arnol'd, V. I. 1984. Catastrophe Theory. Springer-Verlag, New York, 80 pp.

Batchelor, G. K. 1967. An Introduction to Fluid Dynamics. Cambridge University Press, 615 pp.

Böning, C. W. 1986. On the influence of frictional parameterization in wind-driven ocean circulation models. Dyn. Atmos. Oceans, *10*, 63–92.

Boyd, J. P. 1989. Chebyshev and Fourier spectral methods (Series title: Lecture notes in engineering; 49.) Springer-Verlag: Berlin, New York.

Briggs, W. L. 1980. A new class of steady solutions of the barotropic vorticity equation. Dyn. Atmos. Oceans, *4*, 67–99.

Bryan, K. 1963. A numerical investigation of a nonlinear model of a wind-driven ocean. J. Atmos. Sci., *20*, 594–606.

Cessi, P. and G. Ierley. 1993. Nonlinear disturbances of western boundary currents. J. Phys. Oceanogr., *23*, 1727–1735.

Drazin, P. G. and W. H. Reid. 1981. Hydrodynamic Stability. Cambridge University Press, 527 pp.

Godfrey, J. S. 1973. Comparison of the East Australian Current with the western boundary flow in Bryan and Cox's (1968) numerical model ocean. Deep-Sea Res., *20*, 1059–1076.

Halkin, D. and H. T. Rossby. 1985. The structure and transport of the Gulf Stream at 73°W. J. Phys. Oceanogr., *15*, 1439–1452.

Hall, M. M. 1986. Horizontal and vertical structure of the Gulf Stream velocity field at 68W. J. Phys. Oceanogr., *16*, 1814–1828.

Holland, W. R. 1978. The role of mesoscale eddies in the general circulation of the ocean—numerical experiments using a wind-driven quasi-geostrophic model. J. Phys. Oceanogr., *8*, 363–392.

Ierley, G. R. 1987. On the onset of inertial recirculation in barotropic general circulation models. J. Phys. Oceanogr., *17*, 2366–2374.

Ierley, G. R. and W. V. R. Malkus. 1988. Stability bounds on turbulent Poiseuille flow. J. Fluid Mech., *187*, 435–449.

Ierley, G. R. and O. G. Ruehr. 1986. Analytic and numerical solutions of a nonlinear boundary-layer problem. Stud. Appl. Math., *75*, 1–36.

Ierley, G. R. and V. A. Sheremet. 1995. Multiple solutions and advection-dominated flows in the wind-driven circulation. Part I: Slip. J. Mar. Res., *53*, 703–737.

Ierley, G. R. and W. R. Young. 1991. Viscous instabilities in the western boundary layer. J. Phys. Oceanogr., *21*, 1323–1332.

Il'in, A. M. and V. M. Kamenkovich. 1964. The structure of the boundary layer in the two-dimensional theory of oceanic currents. Okeanologiya, *4*, 756–769 (in Russian).

Kamenkovich, V. M. 1966. A contribution to the theory of the inertial-viscous boundary layer in a two-dimensional model of ocean currents. Izvestiya USSR Acad. Sci., Atmos. Oceanic Phys., *2*, 781–792, (translated from Russian).

Kamenkovich, V. M., V. A. Sheremet, A. R. Pastushkov and S. O. Belotserkovsky. 1995. Analysis of the barotropic model of the subtropical gyre in the ocean for finite Reynolds numbers. Part I. J. Mar. Res., *53*, 959–994.

Mallier, R. 1994. On the parametric model of western boundary outflow. Stud. Appl. Math., *91*, 17–25.

Meacham, S. P. and P. S. Berloff. 1997. Barotropic wind-driven circulation in a small basin. J. Mar Res., *55*, (in press).

Miller, A. J., W. R. Holland and M. C. Hendershott. 1986. Open-ocean response and normal mode excitation in an eddy-resolving general circulation model. Geophys. Astrophys. Fluid Dyn., *37*, 253–278.

Morgan, G. W. 1956. On the wind-driven ocean circulation. Tellus, *8*, 301–320.

Munk, W. H. 1950. On the wind-driven ocean circulation. J. Meteorol., *7*, 79–93.

Pedlosky, J. 1987. Geophysical Fluid Dynamics. (Second edition) Springer-Verlag, 710 pp.

Sheremet, V. A., V. M. Kamenkovich and A. R. Pastushokov. 1995. Analysis of the barotropic model of the subtropical gyre in the ocean for finite Reynolds numbers. Part II. J. Mar. Res., *53*, 995–1024.

Sverdrup, H. 1947. Wind-driven currents in a baroclinic ocean: with application to the equatorial currents of the eastern Pacific. Proc. Natl. Acad. Sci. USA, *33*, 318–26.

Veronis, G. 1963. An analysis of wind-driven ocean circulation with a limited number of Fourier components. J. Atmos. Sci., *20*, 577–593.

Whitney, H. 1955. Mapping of the plane into the plane. Ann. Math., *62*, 374–410.